Glacial Meltwater in the Southeast Amundsen Sea: A timeseries from 1994-2020

Andrew N. Hennig[1], David A. Mucciarone[1], Stanley S. Jacobs[2], Richard A. Mortlock[3], Robert B. Dunbar[1]

5 [1]Earth System Science, Stanford University, Stanford, California, 94305, USA
[2]Lamont-Doherty Earth Observatory, Columbia University, Palisades, New York, 10964, USA
[3]Earth and Planetary Sciences, Rutgers University, Piscataway, New Jersey, 08854, USA

Correspondence to. Andrew N. Hennig (ahennig@stanford.edu)

Abstract. Ice sheet mass loss from Antarctica is greatest in the Amundsen Sea sector, where 'warm' deep seawater melts
10 and thins the bases of ice shelves hundreds of meters below the sea surface. We use nearly 1000 paired salinity and oxygen isotope analyses of seawater samples collected on seven expeditions from 1994 to 2020 to produce a time series of glacial meltwater inventory on the Southeast Amundsen Sea continental shelf. Water column salinity-δ^{18}O yield freshwater endmember δ^{18}O values from-30.2‰ to -28.4‰, demonstrating that regional freshwater content is dominated by deep glacial melt. The meltwater fractions display temporal variability in basal melting, with 800 m water column meltwater
15 inventories from 7.7 m to 9.2 m. This result corroborates recent studies suggesting interannual variability in basal melt rates of West Antarctic ice shelves and is consistent with the Amundsen region's influence on ocean salinity and density downstream in the Ross Sea.

1 Introduction

Four decades of observations have shown significant and increasing ice mass loss from Antarctica (Rignot et al., 2011;
20 Velicogna et al., 2014; Rignot et al., 2019). A Special Report on the Ocean and Cryosphere in a Changing Climate (SROCC) projected 0.61 m to 1.10 m of sea level rise (SLR) by 2100 under RCP8.5 forcing, with uncertainty largely hinging on the Antarctic ice sheet (IPCC, 2022). Over the past two decades, losses from the West Antarctic Ice Sheet (WAIS) have comprised 84±12% of the total Antarctic contribution to SLR (1 – 1.2 cm, since 1901; WCRP Global Sea Level Budget Group, 2018), with glaciers flowing into the Amundsen Sea Sector dominating the overall negative mass balance of the ice
25 sheet (Shepherd et al., 2019). High ice shelf basal melt rates there have been linked to the flow of 'warm' modified Circumpolar Deep Water (mCDW) onto the continental shelf and its penetration into sub-ice shelf cavities (Jacobs et al., 1996; Paolo et al., 2015; Pritchard et al., 2012) where it can access ice shelf grounding lines (Rignot and Jacobs, 2002), however estimates of Antarctic SLR contributions from basal melt remain poorly constrained (van der Linden et al., 2021, 2023).

30   While there is evidence for accelerating ice mass loss throughout West Antarctica (e.g. Shepherd et al., 2019) driven largely
by ice shelf basal melt (Paolo et al., 2015; Pritchard et al., 2012), some studies have shown greater interannual variability in
basal melt rates than increase (Paolo et al., 2018; Holland et al., 2019; Adusumilli et al., 2020; Flexas et al., 2022), and some
have even suggested a slowing of basal melt rates (Paolo et al., 2022) and grounding line retreat (Christie et al., 2023). Here
we use a method independent of satellite-based measurements to assess the glacial meltwater (GMW) inventory in the
35   coastal water columns of the SE Amundsen Sea.

Southern Ocean water masses typically have been differentiated and defined by measurements of temperature, salinity, and
less often by including δ^{18}O (Jacobs et al., 1985). Salinity- δ^{18}O relationships can be used to infer the source region and
influence of highly δ^{18}O-depleted zero-salinity glacial freshwater on seawater properties. Where ice shelf basal melting is
40   deep, meltwater oxygen isotope depletion far exceeds that of local ocean surface precipitation. A spatial and temporal array
of samples can thus be utilized to track GMW quantity and distribution, especially in coastal regions where ice shelf melting
is strong. Prior studies have used δ^{18}O measurements to estimate meteoric waters in the Amundsen Sea water column
(Biddle et al., 2019; Jeon et al., 2021; Randall-Goodwin et al., 2015) and elsewhere around Antarctica (Meredith et al., 2010,
2018; Silvano et al., 2018) but so far have revealed little about temporal variability or possible trends in glacial meltwater
45   content. Here, we use nearly 1000 seawater isotope samples collected during seven austral summers from 1994 to 2020
(**Figure 1**) to investigate meltwater sources, water column inventories, and interannual variability in the SE Amundsen Sea.
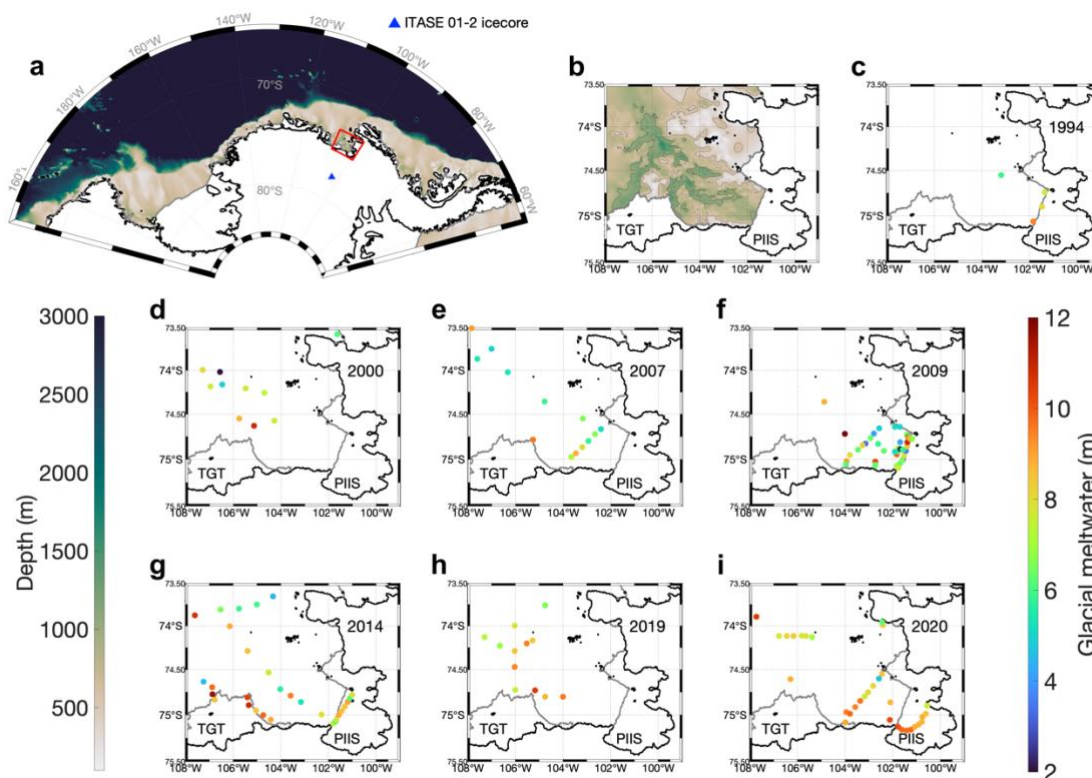
Figure 1: δ¹⁸O sampling locations each year. (a) SE Amundsen study area, and location of the ITASE01-2 ice core. (b) detailed bathymetry of study location (shading), with isobaths at 500 m and 1000 m (lines). (c-i) Colored dots show sample

50 locations, with colors representing vertically integrated glacial meltwater inventories between 0 m and 800 m from 1994 to 2020. Gray lines indicate seaward boundaries of Thwaites Glacier Tongue (TGT) and the Pine Island Ice Shelf (PIIS). Often limited by fast ice, station locations tend to show higher GMW inventories along or near those calving fronts. The former is referenced to 2000 (Schaffer et al., 2014; Fretwell et al., 2013), a relatively stable location before a ~20 km retreat following calving events between 2017 and 2020 (Joughin et al., 2021a). Stations where depth sampling did not extend to the seafloor

55 show only partial water column inventories.

2 Data and methods

1.1 Sample collection and analysis

Samples were collected during 7 field seasons from sites in the SE Amundsen Sea from 1994 to 2020 (**Figure 1**, **Table 1**). Salinity profiles were obtained using calibrated conductivity cells on SBE911 CTDs, monitored with shipboard bottle sample

60 analyses with Guildline AutoSal and PortaSal salinometers. For most years (1994, 2007, 2009, 2014), δ¹⁸O was measured

using an Isotope Ratio Mass Spectrometer (IRMS; Micromass Optima Multiprep or a Finnigan MAT252 HDO). All samples collected in 2019 and 2020, and some in 2007 and 2009, were measured with a Picarro L2140-i Cavity Ring Down System (CRDS). Equivalence has been demonstrated between CRDS and IRMS measurements (Walker et al., 2016; Appendix A7). In all cases, values are reported as per mille (‰) deviations(δ), relative to Vienna Standard Mean Ocean Water (VSMOW2; Coplen, 1994).

Table 1: Summary of $\delta^{18}O$ data sources, sampling intervals, methods & applications

Year	Cruise	Sample collection dates	# Samples	$\delta^{18}O$ Technique(s)
1994	NBP94-02 (Hellmer et al., 1998)	14 Mar. 1994 – 15 Mar. 1994	26	IRMS CO_2 equilibration
2000	NBP00-01 (Jacobs et al., 2002)	16 Mar. 2000 – 20 Mar. 2000	62	IRMS CO_2 equilibration
2007	NBP07-02	24 Feb. 2007 – 27 Feb. 2007	74	IRMS CO_2 equilibration, CRDS
2009	NBP09-01	16 Jan. 2009 – 29 Jan. 2009	175	IRMS CO_2 equilibration, CRDS
2014	iSTAR2014 (Biddle et al., 2019)	5 Feb. 2014 – 20 Feb. 2014	213	IRMS CO_2 equilibration
2019	NBP19-01	12 Jan 2019 – 14 Jan 2019	107	CRDS
2020	NBP20-02	5 Feb. 2020 – 8 Mar. 2020	280	CRDS

Some of the 2009 samples were processed at Rutgers University in 2010 using a Micromass IRMS; the remainder in 2020 using a Picarro CRDS system at Stanford University. While the latter samples had not been opened since collection, a substantial number were compromised by evaporation during 10 years of storage. The 2009 samples analyzed in 2020 were scrutinized visually and newly measured sample densities compared with those derived from the CTD measurements. Data from compromised samples were discarded (Appendix). A subset of 100 samples from 2019 and 2020 were processed concurrently using CO_2 equilibration on a Finnigan MAT252 IRMS and CRDS via vaporizer to ensure data comparability between instrumentation (Appendix A7). IRMS (CRDS) measurements for all years achieved a precision of 0.04‰ (0.02‰) based on replicate analyses.
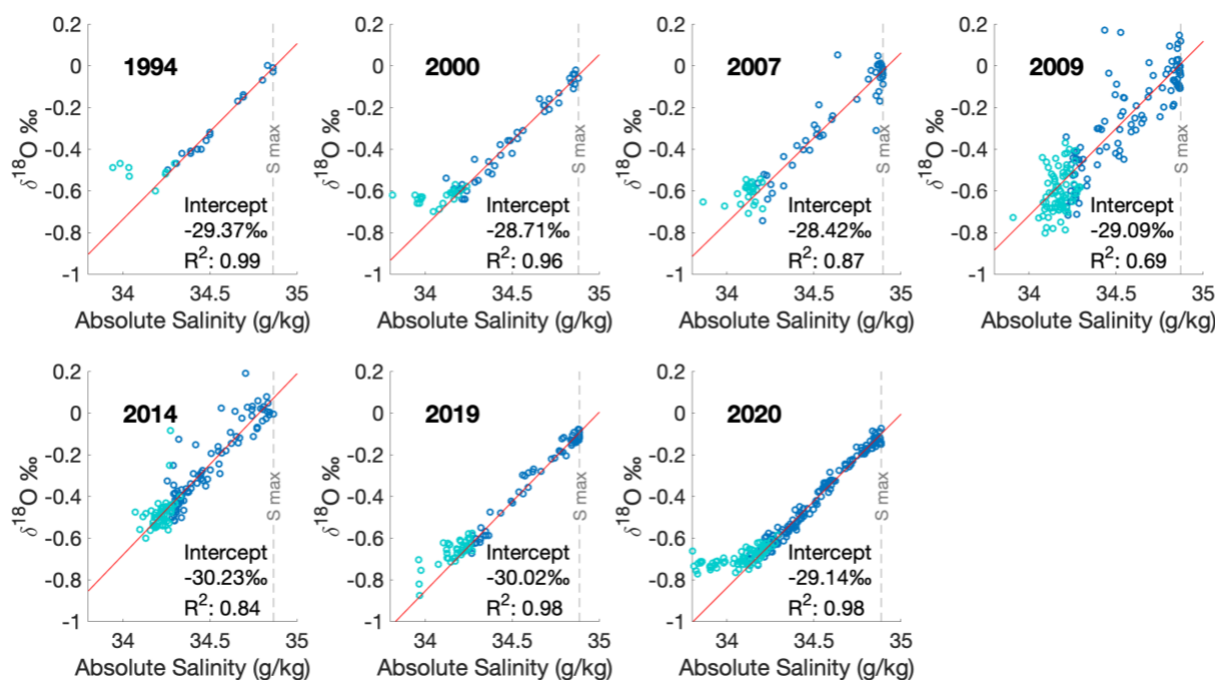
Previous studies (Lécuyer et al., 2009; Skrzypek and Ford, 2014; Benetti et al., 2017) have observed a possible salt effect offset in measured seawater $\delta^{18}O$ using both CRDS and IRMS equilibration methods. Benetti et al. (2017) note this salt effect offset is likely to vary between laboratories and analytical methods. As no salt correction was applied to the originally published (1994, 2000, and 2014) data, we have not applied an offset to samples from 2007, 2009, 2019, and 2020. Here, we

compare calculated GMW fractions (Data & Methods), rather than direct isotope measurements, minimizing any potential issues arising from offsets between laboratories (Appendix A2).

1.2 Meteoric waters defined by the δ¹⁸O – salinity relationship

The zero-salinity δ¹⁸O endmember, defined by data below 200 m, reflects pure meteoric freshwater in the form of ice shelf basal melt (Data and Methods). Freshwater endmembers (intercepts) revealed by salinity-δ¹⁸O relationships over the seven sampled summers differ by <2‰, ranging from -28.4‰ to -30.2‰ (**Figure 2**, **Table 2**). These measurements are consistent with the nearest ice-core (ITASE01-2, from 77.84°S, 102.91°W, **Figure 1a**; Schneider et al., 2006; Steig et al., 2005) with a mass-averaged δ¹⁸O value of -29.8±1.9‰. Ice cores further east have less negative δ¹⁸O values (~-20‰; Thomas et al., 2009), while those further west are more negative (~-40‰; Blunier & Brook, 2001). Local precipitation, in the form of snow collected in early 2019 at 72°S, yielded a δ¹⁸O value of ~-15‰, consistent with previous observations at sea-level from this latitude (Masson-Delmotte et al., 2008). The zero-salinity endmembers extrapolated from the regional salinity and δ¹⁸O observations indicate that freshwater added to the water column is dominated by locally derived GMW, as intimated earlier for the 1994 data (Hellmer et al., 1998).

Figure 2: Salinity vs δ¹⁸O plots for each year. Dark blue circles represent samples deeper than 200 m, fit by linear regression shown as red lines (with R² from 0.69 in 2009 to 0.99 in 1994) that project zero-salinity glacial meltwater endmember intercepts. Light gray dashed vertical lines indicate the modified Circumpolar Deep Water (mCDW) salinity

maxima (**Table 2**). The most negative upper water column seawater $\delta^{18}O$ measurements tend to reach minima between -0.8‰ and -0.5‰. The larger scatter in 2009 and 2014 results likely from sample storage issues (Appendix A6).

100 **1.3 Three-endmember mixing model**

We adapt an approach from Östlund & Hut (1984) that has been applied by others in the Peninsula-Bellingshausen-Amundsen region of West Antarctica (Biddle et al., 2019; Jeon et al., 2021; Randall-Goodwin et al., 2015; Meredith et al., 2010) and near Totten ice shelf (Silvano et al., 2018). Our mixing model assumes that observed $\delta^{18}O$ and salinity values are the result of mixtures of mCDW, sea ice melt, and meteoric waters contributing a range of $\delta^{18}O$ and salinity signatures. 105 Meteoric waters deep below the surface are dominated by ice shelf basal melt, but moving toward shallower depths in the water column, will also include wall melt, and iceberg melting; near-surface waters will contain some amount of local precipitation.

Equations 1-3: Three-endmember mixing model. The 3-endmember mixing model uses the absolute salinity and $\delta^{18}O$ of mCDW, sea 110 ice melt, and meteoric water endpoints to solve for the relative abundance of the three water masses in each sample analyzed.

$$f_{sim} + f_{met} + f_{mcdw} = 1 \tag{1}$$
$$f_{sim} * S_{sim} + f_{met} * S_{met} + f_{mcdw} * S_{mcdw} = S_{obs} \tag{2}$$
$$f_{sim} * \delta_{sim} + f_{met} * \delta_{met} + f_{mcdw} * \delta_{mcdw} = \delta_{obs} \tag{3}$$

115 f = fraction of water source

S = salinity

δ = $\delta^{18}O$

sim = sea ice melt

met = meteoric water

120 $mcdw$ = modified circumpolar deep water

obs = observed sample

The primary fraction of interest is that of ice shelf basal and wall meltwater fractions, defined at the zero-salinity intercepts on $\delta^{18}O$-salinity plots of all samples taken each year (**Figure 2**). Below the surface mixed layer, more generally influenced 125 by sea ice melt and local precipitation, the $\delta^{18}O$-salinity plots yield mixing lines with mCDW as the saltiest, least-depleted component, and glacially-derived meteoric water as a highly depleted freshwater endmember. The zero-salinity intercepts extrapolated from these lines represent the mean $\delta^{18}O$ properties of basal ice being melted by warm mCDW. This approach differs somewhat from other studies (Biddle et al., 2019; Meredith et al., 2010) that estimate meteoric water content from approximate glacier $\delta^{18}O$ values.

130

Interannual changes in mCDW inflow will result from variable wind forcing (Dotto et al., 2019; Holland et al., 2019; Kim et al., 2021), combined with on-shelf lateral and vertical mixing. While mCDW incorporates a range of salinities, temperatures, and δ^{18}O values, in the Amundsen Sea it is the warmest, saltiest, and deepest water mass. In the 3-endmember mixing model, mCDW and meteoric waters are defined separately for each year (**Table 2**) based on the δ^{18}O values at the salinity maximum

135 (Biddle et al., 2017) and 0-salinity intercept on the mCDW-glacial meltwater mixing line (**Figure 2**). Sea ice endmember isotopic values adopted from previous studies in the Amundsen and Bellingshausen region(Randall-Goodwin et al., 2015; Meredith et al., 2008) are based on the δ^{18}O of surface water with an offset to account for isotopic fractionation (~+2.1‰) due to freezing.

140 **Table 2: Salinity and δ^{18}O values used in the 3-endmember mixing model**. mCDW and meteoric components are defined independently using the mCDW-GMW mixing line produced from salinity and δ^{18}O observations for each year, as the salinity maximum and 0-salinity intercept, respectively (**Figure 2**; Appendix A1). Sea ice melt uses single values for each year.

Year	mCDW Absolute mCDW Salinity (g/kg)	mCDW δ^{18}O (‰)	Meteoric water (GMW) δ^{18}O (‰)	Sea ice melt salinity (g/kg)	Sea ice melt δ^{18}O (‰)
1994	34.86±0.02	-0.01±0.02	-29.37±1.63		
2000	34.88±0.01	-0.05±0.02	-28.71±0.91		
2007	34.90±0.01	-0.02±0.02	-28.42±0.84		
2009	34.87±0.01	0.01±0.02	-29.09±0.60	7	2.1
2014	34.86±0.01	0.07±0.02	-30.23±0.77		
2019	34.89±0.003	-0.09±0.01	-30.02±0.79		
2020	34.89±0.01	-0.10±0.01	-29.14±0.49		

3 Results

145 ### 1.4 Deep introduction of GMW is consistent with subglacial melt

A 3-endmember mixing model of mCDW, sea ice melt, and meteoric water can be used to determine the constituent freshwater components of seawater (**Equations 1-3**) at all depths sampled in the water column (**Figure 3**). We compare the derived GMW fractions that are calculated from separately defined mCDW and GMW values for each year. Using mCDW and GMW endmember values based on annual data mean the calculated GMW fractions are extremely unlikely to be

150 impacted by analytical calibration offsets between laboratories (Data and Methods; Appendix A2).
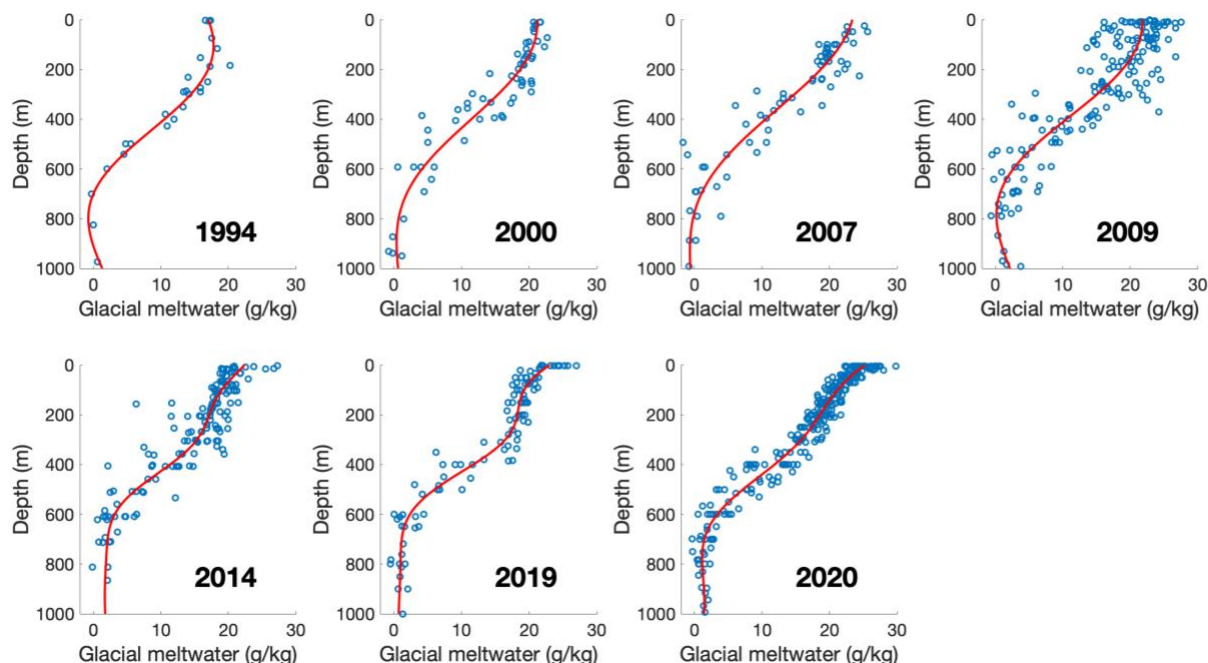
Figure 3: Glacial meltwater fractions (g/kg) in the SE Amundsen Sea water columns. Red lines represent Gaussian Process regression fits. Small negative GMW values at depth in some years are mathematical artifacts that occur when the sample $\delta^{18}O$ is higher than that of the mCDW endmember (**Table 2**, Data and Methods).

Evidence of highly $\delta^{18}O$-depleted freshwater is found at depths shallower than 800 m, increasing rapidly upward from ~600 m to the surface or its mixed layers (**Figure 3**). The mean depth of the Pine Island Ice Shelf calving front was about 400 m in 2009 (Jenkins et al., 2010). Outflows from such depths, lightened by the addition of GMW, rise through denser waters above, along ice shelf calving fronts (Dierssen et al., 2002; Mankoff et al., 2012; Thurnherr et al., 2014; Fogwill et al., 2015). Depending on the extent of mCDW heat remaining after basal melting, that will contribute to the formation of coastal polynyas (Mankoff et al., 2012) and surface layer $\delta^{18}O$ minima. Where GMW ends up in coastal water columns depends on its production rate, impact on the density of circulating water, and access of return flows to the ice shelf calving fronts.

1.5 Average GMW inventory over the last two decades

Regional average GMW column inventories were estimated by depth integrating the Gaussian Process fit of the calculated meteoric water fractions (red lines in **Figure 3**). The average GMW inventory was relatively low in 1994 and high in 2000 and 2020, with an uncertainty of ≤0.7 m in an overall average of 8.60 m; ~1% the upper 800 m water columns. Though largely a product of the low GMW inventory in 1994, a linear regression of the mean GMW inventories produces a modest increase of 0.02 m/y. Observations indicate the mCDW responsible for basal melt does not exhibit significant seasonal

8

variability in this region (Mallett et al., 2018), and A related study showed mostly invariable overall melt rates during austral
170 summer (Kimura et al., 2017), when the samples used in this study were collected (**Table 1**).
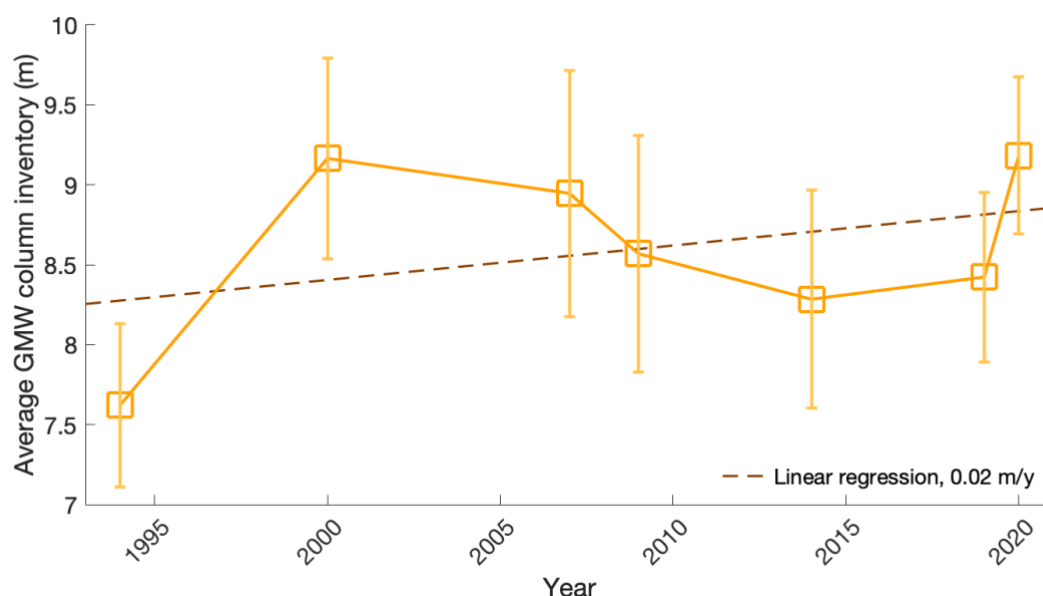

Figure 4: Average GMW column inventory in study area. Depth-integrated GMW volume from the Gaussian Process fit
(see **Figure 3**) between the sea surface and 800 m depth. Error bars show the uncertainty in mean GMW column inventory
175 associated with analytical precision and uncertainty in endmember values (Data and Methods). A linear regression of the
mean values shows an average increase of 0.02 m/year.

1.6 Uncertainty analyses

To account for sampling location variability between years, we assessed sensitivity of the mCDW signature and average
meltwater inventory to sampling location. The greatest geographic variability in mCDW δ^{18}O was measured in 2014, when
180 the total spread was 0.03‰ (σ 0.01‰) – well within analytical precision for both CRDS and IRMS (Appendix A7).
Although the mixing model employs a single salinity and δ^{18}O value for mCDW each year, mCDW exhibits a relatively
small range in properties, both spatially and temporally.

Comparing GMW content and δ^{18}O-salinity relationships between different groups of stations, we found that sample location
185 variability had an insignificant impact on calculated average meteoric water content, except for 2014, when the stations
along the edge of TGT had considerably higher GMW content. In the interest of improving interannual comparability, 2014
stations closest to TGT were excluded from the average GMW content analyses (Appendix A4).

190 We used 10,000 Monte Carlo simulations on each data point to test for sensitivity to variance in mCDW properties, endmember uncertainty, and analytical precision in the 3-endmember GMW fraction model. Each observed value and water mass endpoint was varied around the reported value by the analytical and environmental uncertainty associated with that tracer (Appendix A3). Zero-salinity intercept (meteoric endmember) uncertainty associated with analytical precision ranges from ±0.48‰ in 2020 to ±1.62‰ in 1994, varying inversely with the number of data points available for the extrapolation. Uncertainty in GMW fractions was ±1.5 – 1.7 g/kg, corresponding to ±0.5 – 0.7 m (±6 - 8%) mean water column GMW

195 inventory (Gaussian Process fit, red lines in **Figure 3**; Appendix A3) with 2009 exhibiting the greatest uncertainty, and 2020 the least. Calculated GMW fractions are most strongly influenced by changes to the mCDW endmember, which comprises >95% of the mixture at any given location.

4 Discussion

In this study, we estimate average water column Glacial Meltwater in the SE Amundsen Sea using seawater oxygen isotopes

200 and salinity in a three-endmember mixing model. We defined mCDW and GMW signatures separately for each data year and compare GMW fractions rather than $\delta^{18}O$ values. This this limits way any systematic isotopic offsets between laboratories from affecting the year's calculated GMW fractions (Appendix A2). The results of this study show local meltwater content varying from a low of 7.6 m in 1994 to a high of 9.2 m in 2020. Between 2000-2020, inventories fluctuate, without an apparent trend. Several other studies have also shown relatively stable basal melt rates, fluctuating

205 interannually in this region of Antarctica (Paolo et al., 2018; Holland et al., 2019; Adusumilli et al., 2020; Flexas et al., 2022).

Basal melt in the Amundsen Sea sector is driven by the thickness of the mCDW layer transported on-shore, rather than its temperature (Dutrieux et al., 2014; Jenkins et al., 2018). The thickness of the mCDW layer is controlled by local wind

210 forcing of a shelf break undercurrent, coupled to the Amundsen Sea Low. Changes in local wind forcing have decelerated the local undercurrent, decreasing the thickness of the mCDW layer and reducing the heat transport onto the shelf and resulting in an overall cooling of Amundsen Sea shelf waters from 2010 through 2016 (Dutrieux et al., 2014; Webber et al., 2017; Jenkins et al., 2018; Dotto et al., 2020). Grounding line retreat of PIIS and TWG had been accelerating, but experienced a slowdown between 2010-2015 relative to the preceding period driven by changes to offshore winds (Christie

215 et al., 2023). Our inventories show a local high in 2000, and a local low in from 2009 – 2019. A recent modelling study showed an increase in PIIS and TWG basal melt between the early 1990s and 2000, followed by relative stability thereafter (Flexas et al., 2022). Our results show an increase in average GMW after 1994, followed by interannual fluctuation from 2000-2020, with average GMW inventories remaining well above 1994 levels. Assuming steady-state ocean circulation strength, the relatively steady GMW inventories are consistent with the linear, longer-term freshening trend reported

220 downstream in the Ross Sea (Jacobs et al., 2022).

We calculate average GMW inventories from the surface to 800 m. In most years, there is a tendency for the maximum integrated GMW volume to extend westward from the SW corner of the PIIS, and along the Thwaites Glacier Tongue (TGT), consistent with the gyre-like circulation in the area between PIIS and TGT . This pattern of GMW distribution is

225 consistent with that previously observed using traditional hydrographic tracers (Naveira Garabato et al., 2017). Roughly half of the total meltwater inventory is in the upper 200 m, and inventories below that depth yield the same general trend in interannual variability (Appendix A5), indicating that the observed variability is indeed indicative of basal melt, and not merely an artefact of local interannual variability in precipitation. A spatial sensitivity analysis also shows no significant impact of year-to-year variation in sampling locations on average GMW inventory (Appendix A4).

230

The Amundsen Sea sector receives 0.5 m – 1 m (water equivalent) of precipitation each year (Donat-Magnin et al., 2021) and the residence time of deep shelf waters in this region is ~one year (Tamsitt et al., 2021). With a local precipitation δ^{18}O of -15‰, even an entire year's precipitation remaining in the upper water column at the time of sampling would only account for ~3% - 7% of the overall column inventories (Appendix A5). Furthermore, a substantial fraction of local

235 precipitation will be deposited on sea-ice, much of which is subsequently advected out of the study area (Assmann et al., 2005). While previous studies (Biddle et al., 2019; Meredith et al., 2010) have excluded the upper water column due to uncertainty surrounding local precipitation, our results suggest realistic glacial meltwater content can still be estimated in near-surface seawater.

5 Conclusion

240 We used a time-series of seawater δ^{18}O and salinity collected in the SE Amundsen Sea from 1994 to 2020, using salinity and δ^{18}O to calculate water column inventories of GMW. The average water column inventory of GMW was lowest in 1994 and highest in 2000 and 2020, with enough uncertainty in meltwater inventories and interannual variability to render a linear increase of 0.02 m/y statistically insignificant. These results align with recent studies showing relative stability and interannual variability in basal melt rates in this region. Our results also suggest a lower melt period through the 2000s,

245 followed by the highest melt year in 2020.

The WAIS is an important region for understanding future global sea level rise, particularly with increasing ocean temperatures driving basal melt and increasing the flow of its ice streams into the sea. More recent remote-sensing and modelling studies are more indicative of interannual variability than acceleration in WAIS melt. The meltwater inventories

250 calculated here from seawater δ^{18}O observations also suggests a relatively stable basal melt rate in the SE Amundsen Sea, with interannual fluctuations potentially masking an increase over 2.6 decades. These results demonstrate the independent utility of seawater δ^{18}O data in monitoring and helping to better constrain satellite-based estimates of basal melt and glacial

change. Integration of δ^{18}O data into numerical models should further our understanding of ocean circulation strength and ice loss along this climatically sensitive sector of the WAIS. Continued sampling for δ^{18}O in this region could also reveal if and when our measured rates of meltwater volume, already consistent with downstream freshening, rise significantly above the observed short-term variability.

APPENDIX

A1 Defining mCDW

260 Modified Circumpolar Deep Water (mCDW) is one of three endmember waters used in a mixing model to determine glacial meltwater fractions. As the salinity and $\delta^{18}O$ of mCDW are well observationally well constrained and display interannual variability, mCDW properties are defined separately for each year. Error! Reference source not found. illustrates that p rocess, using 2020 data. Being the warmest, saltiest water on the continental shelf, mCDW appears at the top-right on a T-S diagram (Panel a), where it also identifies waters that are least-depleted in $\delta^{18}O$.

265

In Panel b, the same data are plotted, with the y-axis showing $\delta^{18}O$, and the colors indicating temperature. The red (blue) dashed lines show property mixng lines between mCDW and glacial meltwater or sea ice melt, with the colder waters being fresher and more depleted.

270 Panel c covers the same dataset, but with colors illustrating depth. Most data lie above ~800m, with the least $\delta^{18}O$ depletion in a few deeper depressions. Waters are diverted off the mCDW-GMW mixing line in the upper 200 m of the water column, influenced by sea ice melting and atmospheric processes. Sea ice melt will freshen saltier waters but has a slightly positive (+2.1‰) $\delta^{18}O$, while GMW has a very negative $\delta^{18}O$ (~-29‰). Its influence makes resultant mixtures fresher, but somewhat counterbalances the strong negative $\delta^{18}O$ of GMW.
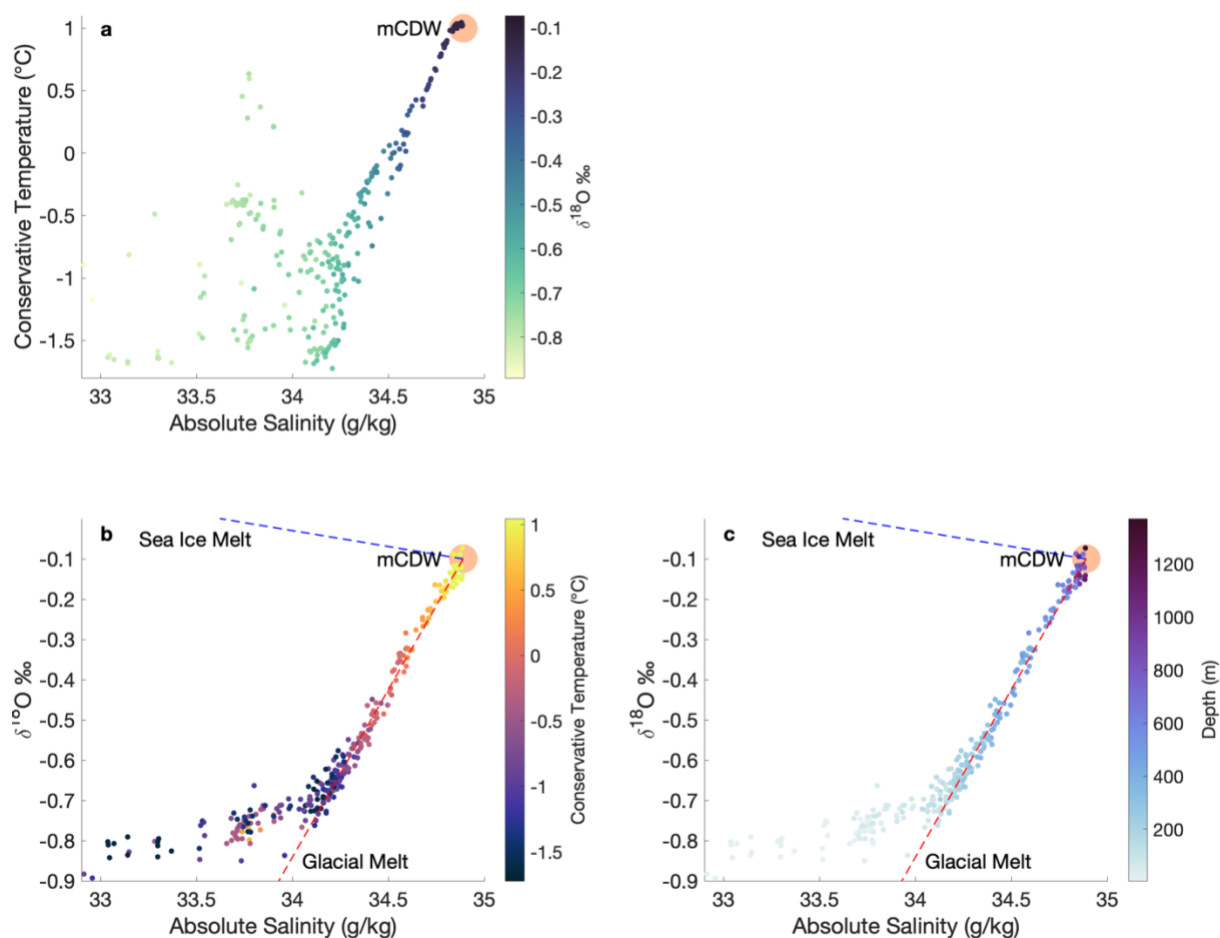
275

Figure A1: Temperature, salinity, and δ¹⁸O from 2020 data. a) T-S diagram with colorbar showing δ¹⁸O. b) δ¹⁸O vs salinity with colorbar showing temperature. c) δ¹⁸O vs salinity with colorbar showing sample depth. The most saline samples are also the warmest, deepest, and least-depleted in δ¹⁸O. Data diverges from the mCDW-glacial melt mixing line at depths shallower than 200 m due to the presence of sea ice melt in the admixture. In Panels b and c, dashed lines show the associated property mixing lines for mCDW mixing with sea ice melt, or GMW.

In **Figure 2** of the main text, δ¹⁸O-salinity plots for each year reveal several data points near the the salinity maximum, with some variability in the corresponding δ¹⁸O. Using only data from below 200 m, trendlines that are extrapolated to 0-salinity intercepts define the mCDW and GMW endmemebers used in the mixing model. mCDW and GMW δ¹⁸O are defined as the δ salinity maximum and 0-salinity intercept on the trendline, respectively (**Table 2**). The location of mCDW corresponds to conventional measures of the deepest and warmest waters on the shelf. The calculated 0-salinity intercept values are consistent with the properties of local GMW.

14

A2 Inter-laboratory offsets

290   When using data produced by different laboratories, it is important to be aware of the potential for systematic offsets. Here we have compared calculated meteoric water fractions rather than $\delta^{18}O$ values, with mCDW and GMW signatures defined separately for each year so that any offset will not affect the values of samples from that year relative to their mCDW/GMW signatures. A sensitivity analysis wherein all sample data from a given year were offset, and mCDW/GMW signatures were re-calculated using the offset data. The offset data and endmemebers were used to calculate GMW fractions in the 3-

295   endmember mixing model – sea ice melt values remained static. We found that an inter-lab offset of 5.7‰ was necessary to change the calculated GMW fraction by an amount greater than the analytical (±0.04‰ $\delta^{18}O$, ±0.003 g/kg absolute salinity) and environmental uncertainty based on ice core measurements (±1.9‰ $\delta18O$) and year-to-year variability in mCDW values (±0.06‰ $\delta18O$) associated with the calculation (±1.6 g/kg). Since, inter-lab offsets would not be expected to be greater than 0.1‰ (Walker et al., 2016), any offsets would not be significant when comparing calculated meteoric water fractions.
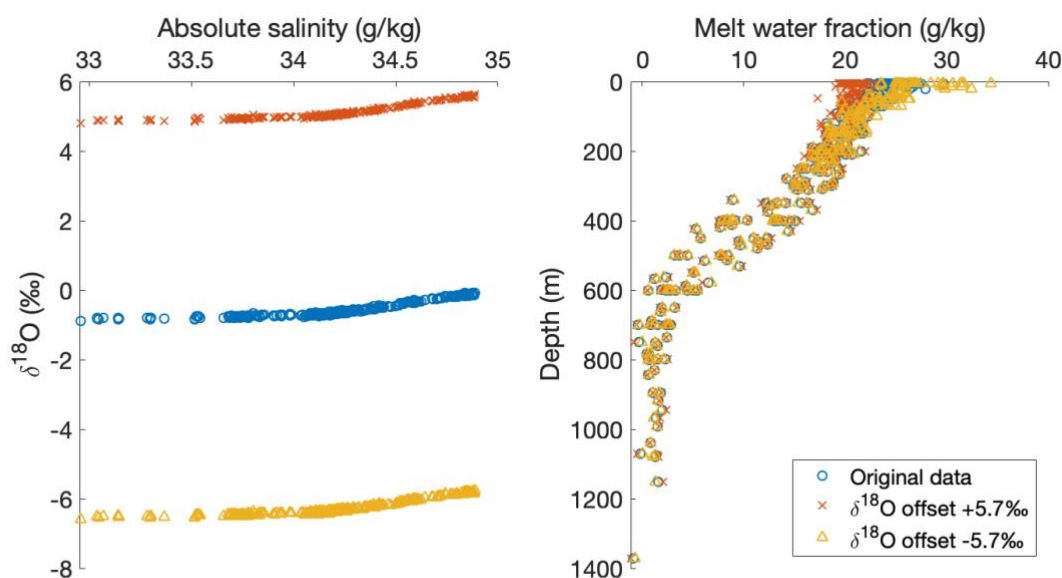
300

Figure A2: Impact on inter-lab offsets on calculated meteoric (glacial melt) water fraction for NBP20-02 data. The left panel shows the $\delta^{18}O$ offset (±5.7‰) necessary to significantly affect calculated GMW fractions. The right panel shows the calculated meteoric water fractions produced using the original, and offset data.

305

A3 Uncertainty in calculated meteoric water fractions

Since meltwater fractions are calculated using analytically-derived measures of salinity and δ^{18}O, the accuracy and precision of these measurements are important. CTD salinity sensors have a reported precision of ±0.002. The IRMS (1994 to 2014) measurements in this study have a reported precision of ±0.04‰ based on replicates, while the CRDS achieved a precision

310 of ±0.02‰. Our end-member values for sea ice melt and meteoric water are largely theoretical. The meteoric endmember is arguably the least-well constrained, with glacial ice in West Antarctica ranging from -20‰ to -40‰, but much of that uncertainty has been eliminated by using the 0-salinity intercept determination on a δ^{18}O-salinity mixing line, corroborated by nearby ice core values, as discussed in the main manuscript. mCDW is the best constrained endmember and is based on many in-situ measurements.

315

We use Monte Carlo simulations to estimate uncertainty in our water mass fraction calculations. We ran 10,000 simulations with values varied randomly within these bounds and represent uncertainty by the standard deviation of the difference between the simulated runs, and the initial run. Each parameter (δ^{18}O, salinity) was varied around the reported endpoints (**Table 2**) and the measured observational values for each of our samples, by the uncertainty associated with environmental

320 variability, and instrument precision (**Table A1**). All observations were randomly perturbed by analytical precision (0.04‰ δ^{18}O; 0.002 g/kg salinity); these perturbations also have an impact the mCDW and GMW endmembers for each run, since they are calculated from observations >200 m. In addition to perturbations made to the observations, endmembers are further perturbed. The perturbation used for the glacial meltwater endmemeber is the standard deviation of the ITASE01-2 ice core. The perturbations for sea ice melt were selected based on theoretical values (Rohling, 2013). mCDW perturbations were

325 selected based on the data distribution for each year. δ18O was varied by the standard deviation associated with the 95% prediction interval produced from the >200m δ^{18}O-salinity relationship at the salinity maximum; salinity was varied by the standard deviation in salinity of the highest δ^{18}O data falling within the 95% prediction interval at the salinity maximum.

Table A1: Endmember perturbations for uncertainty analysis

Endmember	δ^{18}O perturbation (‰)	Absolute Salinity perturbation (g/kg)
Glacial meltwater (meteoric)	1.9	N/A
Sea ice melt	2	0.11
mCDW, 1994	0.010	0.018
mCDW, 2000	0.012	0.011
mCDW, 2007	0.018	0.011
mCDW, 2009	0.021	0.008
mCDW, 2014	0.017	0.013
mCDW, 2019	0.006	0.003
mCDW, 2020	0.004	0.005

330

The mean uncertainty associated with GMW water fractions is $\pm 1.5 - 1.7$ g/kg – this corresponding to of $\pm 0.5 - 0.7$ m average meteoric water column inventory. GMW and Sea Ice Melt fractions vary inversely, while mCDW fractions remain relatively stable. Calculations are most impacted by changes to the mCDW endpoint, as mCDW makes up >951% of the water column any given location.
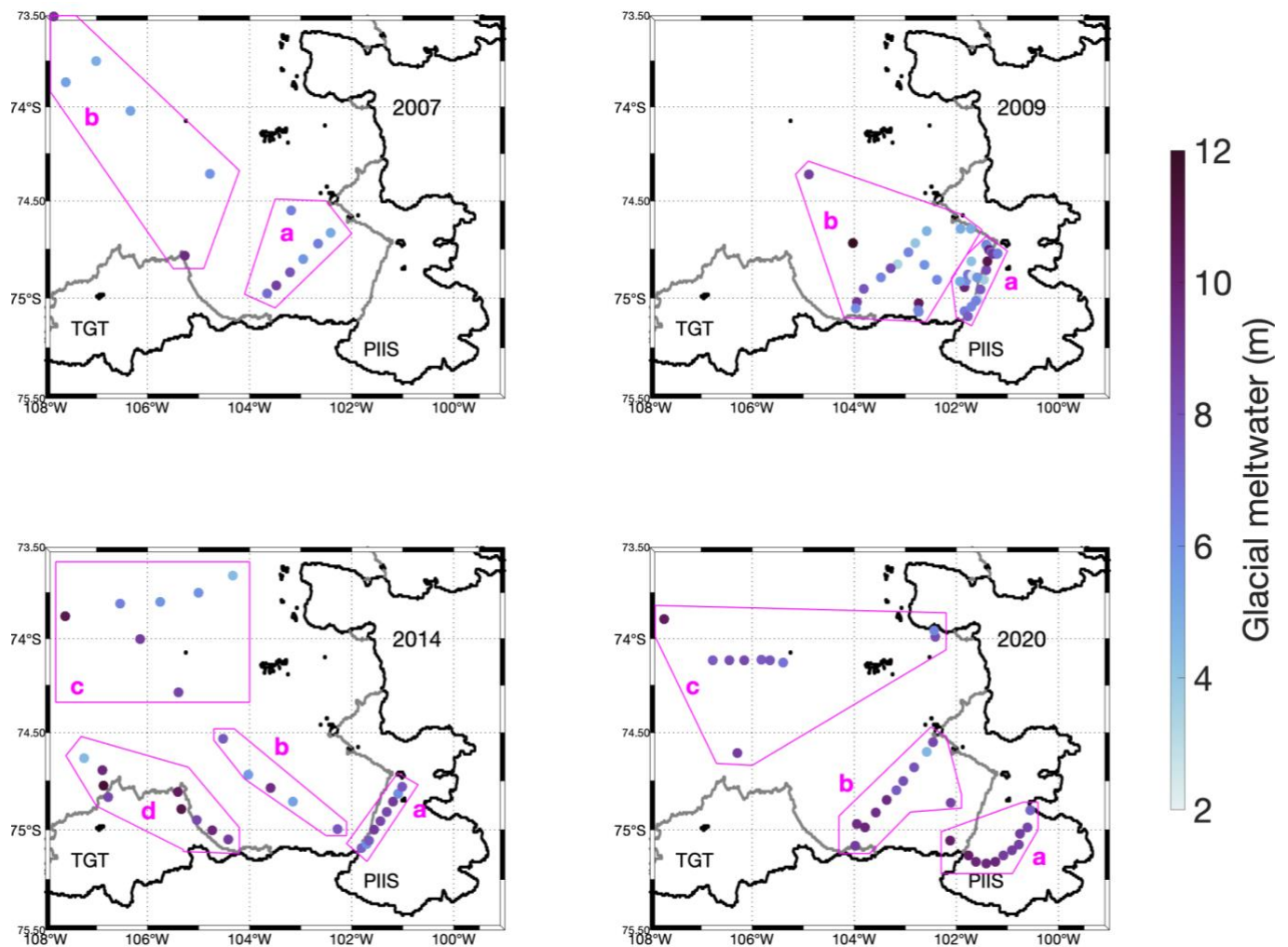
335

For a small number of samples from 2007 (3), 2009 (9), and 2014 (2) the calculated GMW fractions are negative. For the 3 samples in 2007, and 2 in 2009, these figures are within the uncertainty described above. The negative GMW fractions result when high-salinity deep waters were measured to have a δ^{18}O significantly less negative than the mCDW endpoint used in the GMW calculation. The spatial variability in mCDW, is reasonably well constrained year-to-year, with a wider spread in mCDW δ^{18}O for 2007, 2009, and 2014 than in other years. The samples in question may have been subject to evaporation, resulting in a higher δ^{18}O, highlighting the importance of appropriate sample collection and storage.

340

A4 Geographical sensitivity of mCDW signature and meltwater inventory

Figure A3: Sampling locations for 4 years and analyzed data groupings. To understand how much year-to-year differences in sampling location affects mCDW and GMW fingerprinting, and average meltwater inventory calculations, we selected the 4 years with the greatest number of data points and ran these analyses on different geographic groupings of sample data (**Table A2**).

350

Table A2: Results of geographic sensitivity analysis. mCDW is defined as the δ^{18}O value at the salinity maximum falling on the linear regression of all salinity-δ^{18}O measurements deeper than 200m in each group of stations; GMW δ^{18}O is defined as the 0-salinity intercept on that same line. Uncertainty in mCDW δ^{18}O is represented by the 95% prediction interval at the salinity maximum and uncertainty in salinity is manufacturer's stated analytical precision. Average meltwater inventory is the depth integration of the Gaussian fit of all calculated meteoric water fractions within each group, with uncertainty represented as the standard deviation in GMW fractions achieved using 1000 Montecarlo simulations perturbing the observations and endpoints by associated analytical and environmental uncertainty. For each subset of stations, mCDW and GMW used in GMW calculations endmembers are defined using only those data.

Year	Group	mCDW absolute salinity (g/kg)	mCDW δ^{18}O (‰)	GMW δ^{18}O (‰)	Average GMW inventory (m)
2007	a	34.87±0.01	0.01±0.03	-32.28±1.16	8.8±0.8
	b	34.90±0.01	-0.05±0.02	-25.88±1.36	8.5±0.9
2009	a	34.87±0.01	0.02±0.03	-29.02±0.76	8.5±0.8
	b	34.87±0.01	-0.01±0.05	-28.52±1.07	8.7±1.3
2014	a	34.83±0.01	0.06±0.02	-31.68±1.08	7.5±0.6
	b	34.84±0.01	0.04±0.03	-31.80±1.78	7.7±0.6
	c	34.86±0.01	0.04±0.04	-26.65±1.36	8.4±1.2
	d	34.87±0.01	0.07±0.02	-31.96±1.05	10.1±0.7
2020	a	34.85±0.01	-0.13±0.01	-29.69±0.73	8.5±0.5
	b	34.86±0.01	-0.12±0.01	-29.54±1.05	8.7±0.6
	c	34.89±0.01	-0.11±0.01	-28.21±0.80	8.7±0.6

355

mCDW δ^{18}O (as defined in Section A1, above) was shown to not be geographically sensitive. Surprisingly, in 2007, mCDW defined using only the stations closest to the ice shelf (Group a) produced the least negative δ^{18}O values for mCDW. Since the mCDW closest to the ice shelf is the water that will be melting the ice shelf, and samples from both locations fall on the same δ^{18}O-salinity mixing line, this is not thought to be a problem for our analysis. In all other years, the greatest variability

360 in mCDW δ^{18}O was in 2014, with a total spread of 0.03‰ (st. dev. 0.01‰) – well within ±0.04‰ (0.02 ‰) instrument precision for IRMS (CRDS).

As with mCDW, we see little geographical impact on the calculated average meteoric water column inventory. In almost all cases, the small differences in geography are well below the uncertainty of the calculations. The one exception is 2014,

365 where the stations nearest the Thwaites Glacier Tongue (TGT) exhibit significantly higher meteoric water content than the rest of the study area. While this is consistent with known circulation in the area (Jenkins et al., 2010; Thurnherr et al., 2014; Naveira Garabato et al., 2017; Joughin et al., 2021b), we do not have comparable samples from other years, so those stations were excluded for the purposes of interannual comparisons.
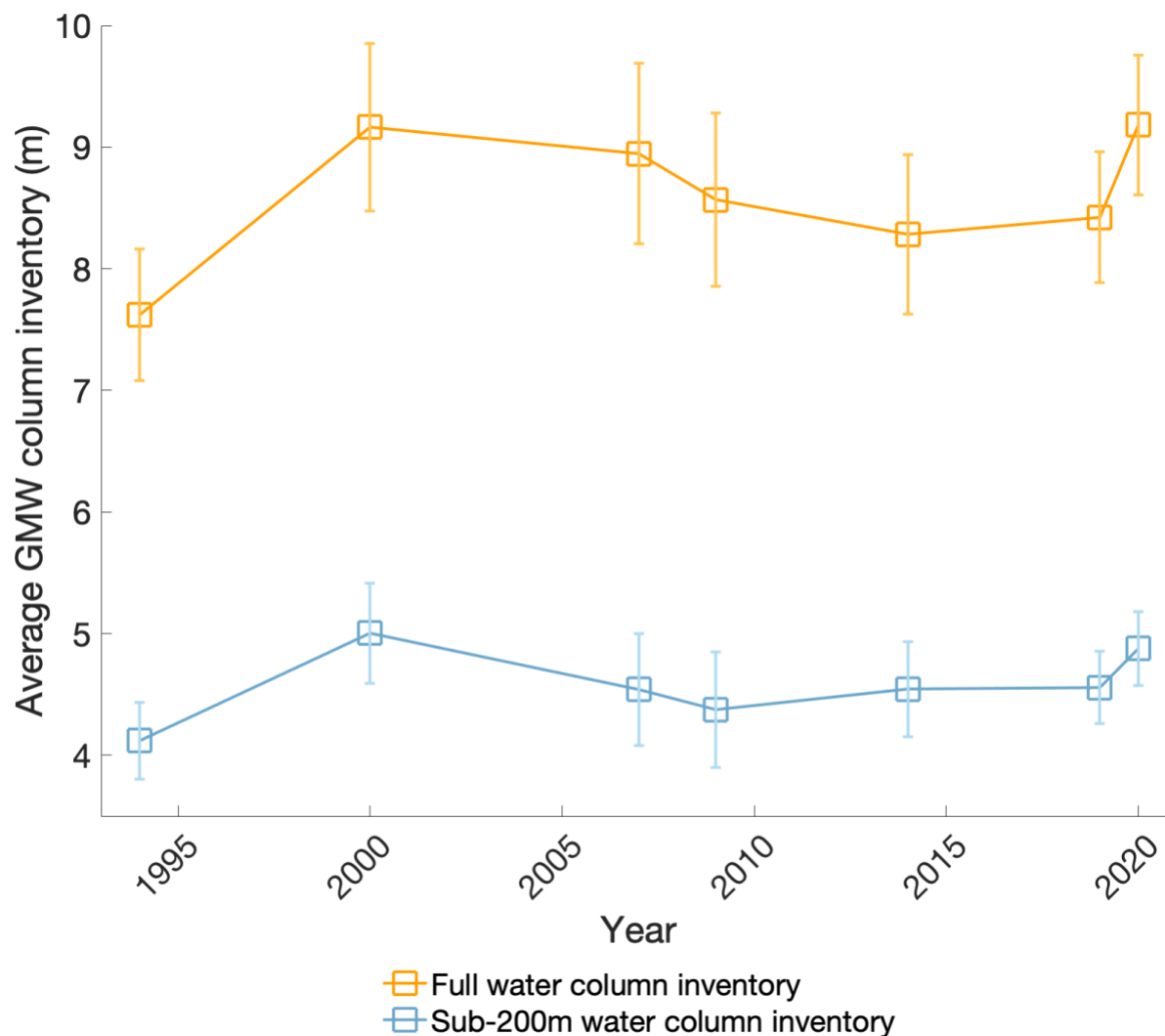
A5 On measuring precipitation in surface waters

The size of the meteoric water fraction calculated using the three-endmember mixing model is inversely proportional to the (negative) magnitude of the meteoric water endmember, as a -15‰ endmember will produce ~1.8x the calculated meteoric water fraction of a -29‰ endmember. For a given mixture, it would thus take ~2x as much -15‰ water to produce the δ^{18}O signature than for -29‰ water.

Sea-level precipitation at this latitude has δ^{18}O values of ~-15‰ (snow collected at 72°S during NBP19-01). This region of the Amundsen Sea receives ~0.5 m water equivalent of precipitation per year (Donat-Magnin et al., 2020). In an extreme case, we could assume that the entirety of 1 year's 0.5 m of precipitation is present in the upper water column at the time of sampling. Given the mathematical relationships above, that would result in a ~0.28 m overestimation of the total glacial meltwater. The lowest (highest) year for average meltwater column inventory 1994, 7.7 m (2020, 9.2 m) corresponds to only a 3.6% (3.0%) overestimation. Even assuming the highest snowfall rates in the region (~1m water equivalent near Abbot and Getz Ice Shelves; Donat-Magnin et al., 2020) this results in an overestimate of <8%. The largest impact of uncertainty around precipitation is thus lower than uncertainty associated with analytical precision and endmember uncertainty.

Figure A4: Average meltwater column inventory in study area. As **Figure 4** from main text, but also showing meltwater inventory between 200m and 800m. Blue bars represent the depth-integrated meltwater volume from the Gaussian Process fit (red lines in **Figure** 3) between 200 and 800 m depth. Error bars show the uncertainty in mean GMW column inventory associated with analytical precision and environmental variability (Data and Methods). The relative year-to-year inventories here show the same general trend (within uncertainty) as **Figure** 4.

Table A3: Relative Fractions of yearly meltwater inventory at depth, and of full water column. Reported column inventories are the depth integration of the Gaussian fit of all measurements in the field area between the specified depths. The Relative fraction is the normalized relative volume of the average inventory compared year to year.

Year	0 m – 800 m Column Inventory, GMW (m)	0 m – 800 m Relative fraction	200 m – 800 m Column Inventory, GMW (m)	200 m – 800 m Relative fraction	Fraction of total GMW in upper 200 m
1994	7.6±0.5	83.0±5.9	4.1±0.3	82.3±6.3	45.9%
2000	9.2±0.7	99.8±7.5	5.0±0.4	100±8.2	45.4%
2007	9.0±0.7	97.4±8.1	4.5±0.5	90.7±9.1	49.2%
2009	8.6±0.7	93.3±7.8	4.4±0.5	87.4±9.4	48.9%
2014	8.3±0.7	90.2±7.2	4.6±0.4	90.8±7.8	45.1%
2019	8.4±0.5	91.7±5.8	4.6±0.3	91.1±6	45.9%
2020	9.2±0.6	100.0±6.3	4.9±0.3	97.5±6.1	46.9%

A6 2009 Sample quality control

A portion of the samples for 2009 were analyzed on an IRMS in 2010, while the rest were stored until a 2020 CRDS analysis. At the latter time, 56% of the samples analyzed contained an unknown precipitate. Several bottles also had a lower than expected sample volume, suggesting evaporation, which would be expected to alter $\delta^{18}O$ through isotopic fractionation. Several steps were taken to ensure the quality of samples analyzed after a decade in storage.

A6.1 SEM EDS Analysis of Precipitate

Samples of the precipitate were extracted from multiple sample bottles and analyzed using a Scanning Electron Microscope, equipped with a FEI Magellan 400 XHR SEM with Bruker Quantax XFlash 6 | 60 SDD EDS detector, at Stanford Nano Shared Facilities (SNSF). Peaks were observed at the spectra associated with Mg, Si, and O, indicating the precipitate is likely some form of Magnesium Silicate Hydroxide ($Mg_3Si_2O_5(OH)_4$), or Magnesium Silicate Hydrate ($Mg_2Si_3O_8 \cdot H_2O$)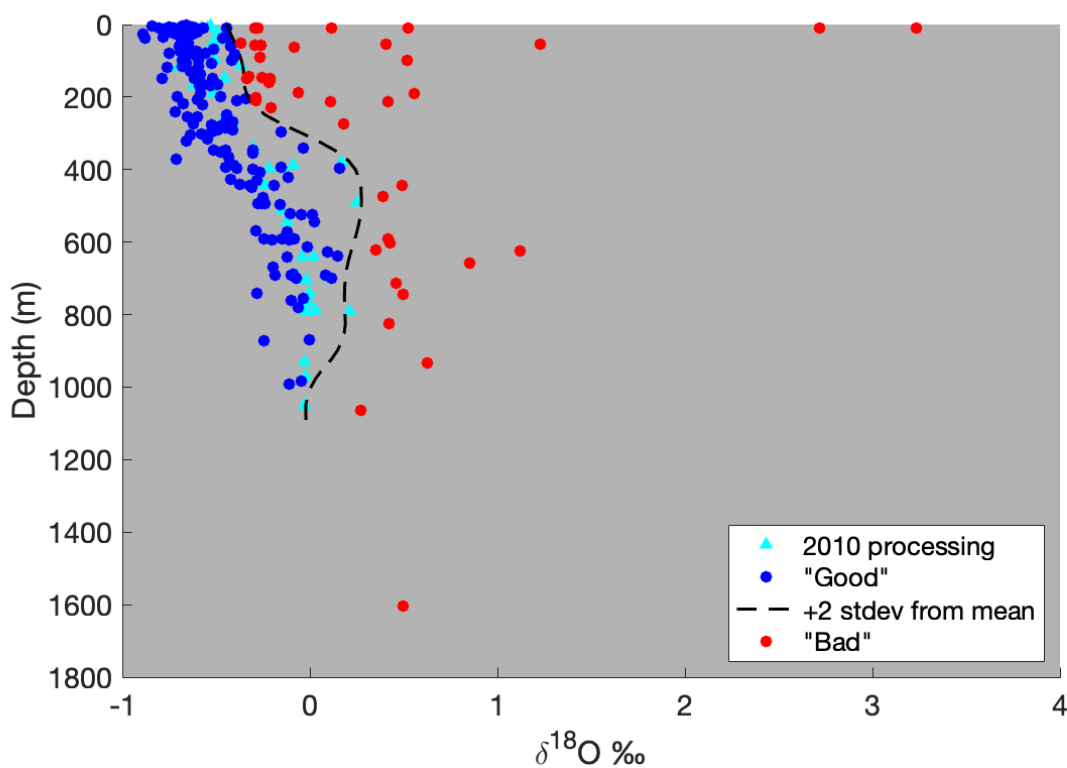. $Si(OH)_4$ is the simplest soluble form of silica and is found universally in seawater at low concentrations (Belton et al., 2012). The maximum amount of silicate that could be expected in this area of the ocean is ~100 µmol/kg (Rubin et al., 1998). In this case, even if the entire 100 µmol/kg of Si were drawn down to 0, solely into a Magnesium Silicate, with a very high fractionation factor, e.g. the -40‰ reported for diatoms (Leclerc and Labeyrie, 1987) the greatest effect on a sample would be 0.0003‰ – well below the analytical precision of the CRDS (0.025‰) or IRMS (0.04‰). Therefore, it is highly unlikely that the precipitate contributed a detectable fractionation or alteration of seawater $\delta^{18}O$ in our samples.

A6.2 Quality control for evaporation
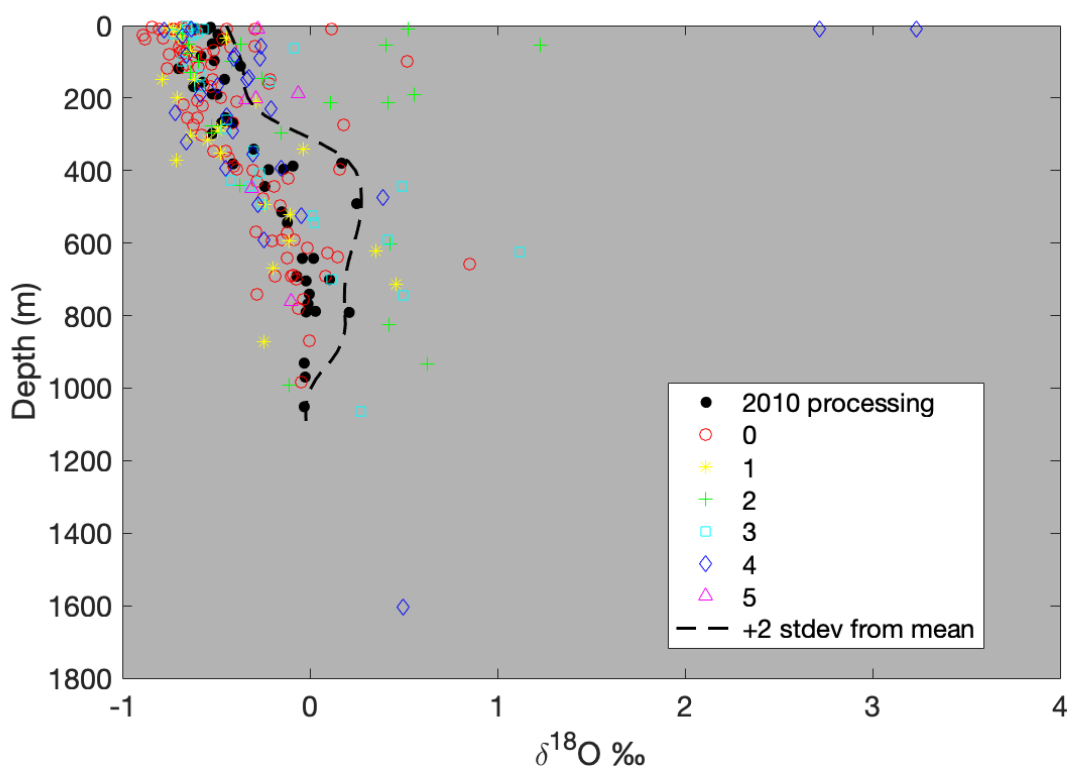
Assuming accurate 2020 analyses, the $\delta^{18}O$ data fall in a broadly predictable pattern, less depleted at depths below ~600m, and more depleted near the surface. Values >2 standard deviations from this pattern denote samples that experienced significant evaporation (**Figure A5**)
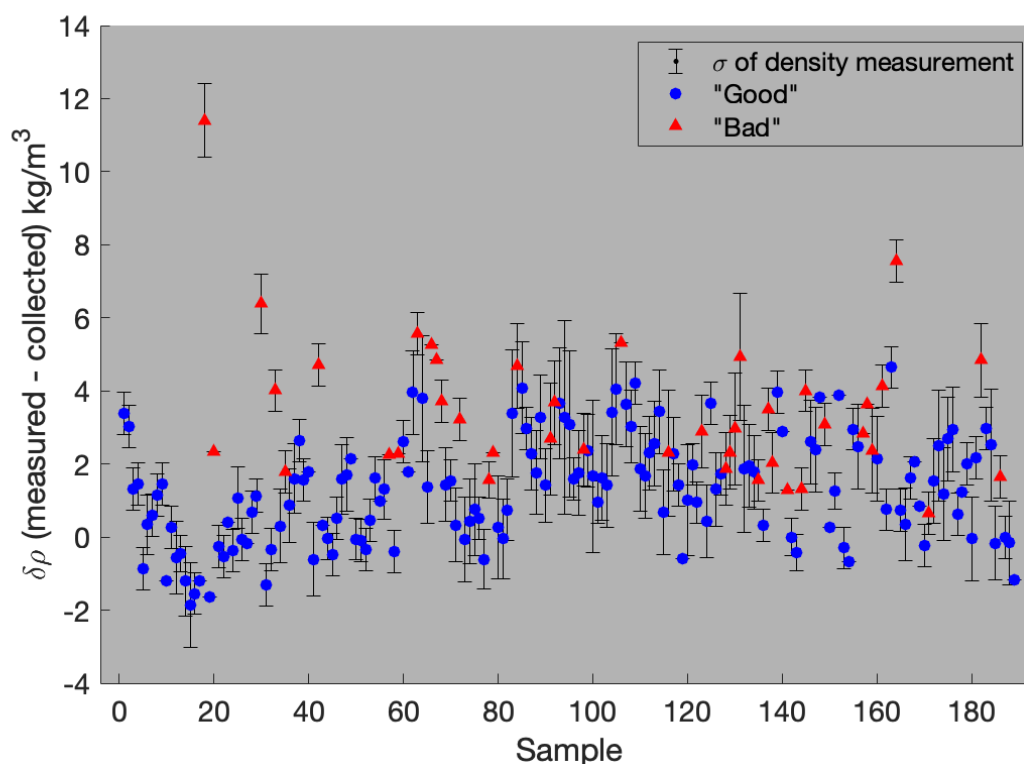

415

Figure A5: $\delta^{18}O$ vs depth for all 2009 samples, coded for likelihood of evaporation. The dashed line represents +2 standard deviations from a moving depth-averaged $\delta^{18}O$ based on the 2010 data, beyond which the results are unacceptable. Archivable data will be made available upon publication.

420   As a secondary check, the $\delta^{18}O$ of all samples was plotted vs depth with a qualitative indicator of the amount of precipitate found in the sample vial (**Figure A6**) to see if any patterns emerged compared to that of depth-comparable samples run in 2010. No clear trend was evident.

23

Figure A6: δ¹⁸O vs depth of all samples, coded by amount of precipitate present. Each bottle was graded by eye based on the volume of precipitate present with 0 being no precipitate present, and 5 being the most precipitate present. As with Figure S3, the dotted line represents +2 standard deviations from the mean $\delta^{18}O$ at each depth.

Evaporation is accompanied by isotopic fractionation, $H_2^{16}O$ evaporates preferentially, leaving the remaining liquid relatively enriched in the $H_2^{18}O$. Evaporation also increases the salinity and thus density of the remaining sample thereby increasing sample density. We measured the density of each seawater sample 5 times using a calibrated 1ml pipet and mg balance. The theoretical density of each sample was calculated from its associated CTD salinity and temperature during weight determination. Differences between measured and theoretical densities for each sample are plotted in **Figure A7**.

Figure A7: Theoretical density is based on CTD salinity at each sample location, and measured density calculated from 1ml sample aliquots weighed on a mg scale, with sample coding as in **Figure A5**. Error bars represent the standard deviation of replicates for each measurement.

While a few samples show clear evidence of evaporation, and correspondingly high $\delta^{18}O$ values, most show less obvious density evidence, exposing the limitations of our scale accuracy at that level. 75% of the samples measured showed a higher than expected density and the remainder measured a lower than expected density. **Figure A7** displays a significant overlap in measured density space between samples previously identified as "good" or "bad" (**Figure A5**). **Figure A7** shows that there are no samples flagged as compromised from our earlier depth-based analysis ("bad") with a $\delta\rho$ greater than 1.3 kg/m^3. At an aggressive first pass, we removed all sample data with a $\delta\rho$ greater than 1.3 kg/m^3 and looked at each hydrocast profile individually, using the remaining data. We then added those excluded samples flagged as "good" back into the dataset, and re-scrutinized individual profiles to check for any qualitative change.

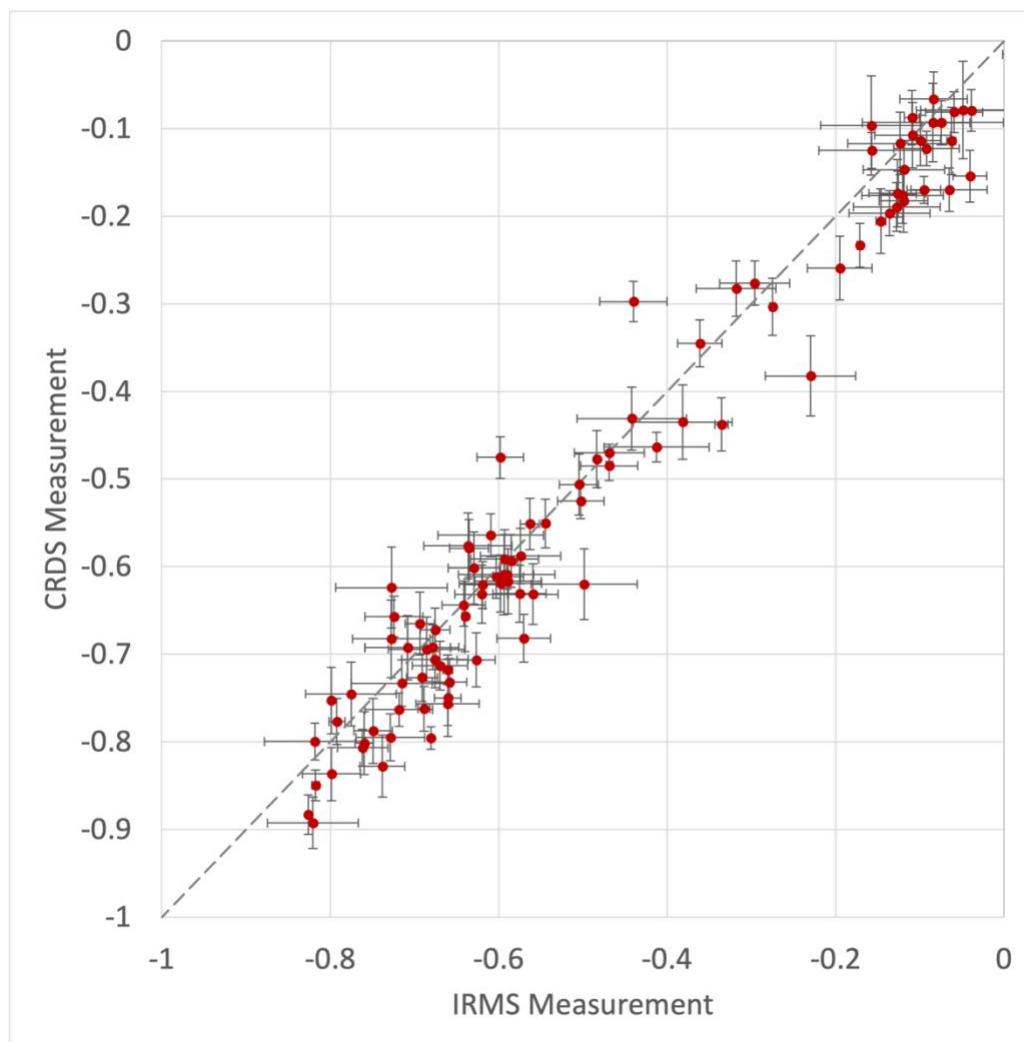**A6.3 Conclusion and final 2009 sample inclusion**

While it is extremely unlikely that the precipitate contributed to a change in sample, some samples do appear to have been subject to evaporation. The inclusion of all samples flagged as "Good" does not qualitatively change the analyses presented

25

in this study when compared with analyses using only those data run in 2010. We exclude 41 samples initially flagged as "Bad," (**Figure A5**) and retain the remaining 148 flagged as "Good".

A7 CRDS and IRMS cross-calibration

We ran 100 samples from 2019 and 2020 concurrently using the Picarro L2140-i CRDS, on a Finnigan MAT252 IRMS (**Figure A8**) using CO_2 equilibration (Epstein and Mayeda, 1953). Both instruments were independently calibrated using international standards VSMOW, SLAP, and GISP, and all samples were run in duplicate. The data from both machines was comparable, with the Picarro achieving a precision of 0.02‰ on replicates, and the IRMS achieving a precision of 0.03‰ on replicates. On average the offset between the CRDS data and IRMS data was -0.02‰, with the CRDS data being more negative than that from the IRMS. Since the offset between the two machines was less than either instrument's precision, data from the CRDS was used as-is. The values reported for the CRDS are the average of 6 individual injections/measurements from each vial; precision is reported based on the standard deviation between multiple 6-injection averages from replicate analyses, separated by days, weeks, or months.

Figure A8: 101 seawater $\delta^{18}O$ samples collected in 2019 and 2020 analyzed with both CRDS and IRMS. Each point represents the value obtained by measuring the same sample on the IRMS (x-axis) and the CRDS (y-axis). Horizontal error bars represent the standard deviation of the IRMS measurements, and vertical error bars represent the standard deviation of the CRDS measurement. The dashed grey line is a 1:1 slope.

A8 CRDS Methods

A large number of isotope samples for this study were run on a Picarro L2140-i CRDS system, rather than a traditional IRMS. Using this system, we were able to achieve an average precision of <0.02‰ on multiple replicate analyses. The instrument setup used was as follows:

- A single standard or unknown run consists of 7 injections (measurements) per sample
- Sample injection volume 2.2 µl

- 3x 5µl rinses with fresh water from inkwell (IW) between each sample
- 3x 2.2µl rinses with sample before first measurement of new sample or standard vial
- Rinse only between sample vials, or 1 rinse for every 7 standard or unknown injections.

In addition to the above instrument method, several protocols were followed with regards to sample and instrument handling.

475
- Fresh vial of internal lab standard (ILS) used each day. The ILS was prepared to have a $\delta^{18}O$ in the middle of the range expected from the unknowns (i.e. ~-0.3‰) to minimize memory issues between samples. The IW was also filled with water of approximately this composition.
- A fresh 2ml vial of ILS was used each day, and discarded at the end of the sequence.
- Samples were pipetted from sealed 10ml or 30ml serum into 2ml vials for analysis on the day they were to be analyzed. The 2ml vials used for analysis were found to only reliably preserve sample $\delta^{18}O$ for <1 week.

480
- After each sequence, the syringe was cleaned with DI water, and then rinsed thoroughly with water from the Inkwell, to minimize memory/contamination issues of residual water left in the syringe.
  - Treated in this way, syringes can be expected to last 1500 to 2500 injections
- Fresh vaporizer septa (part number) was used every day

485
- ILS were analyzed no less than every 5th unknown, and no fewer than 3 ILS were measured per run
- All data were corrected based on the slope of the ILS measurements over the course of the sequence.
- Each run began with no fewer than 10 injections from the IW, to allow the instrument to reach baseline.
- Syringe cleaned thoroughly with DI water each day, and manually rinsed with IW water prior to sequence.
- No more than 5 unknowns (7 injections each) measured between run of ILS (7 injections)

490
- ILS measured at least 3 times during each sequence – at the beginning, end, and midpoint. least 3 standards measured during each sequence.

A typical 24h sequence ran 16 unknowns. The sequence was set up, as follows:

- 15 injections from IW
- ILS (7 injections)

495
- 4 unknowns (4x7 injections)
- ILS (7 injections)
- 4 unknowns (4x7 injections)
- ILS (7 injections)
- 4 unknowns (4x7 injections)

500
- ILS (7 injections)
- 4 unknowns (4x7 injections)
- ILS (7 injections)

Overall, this sequence consists of 162 injections, 112 of which contained salt, for a vaporizer load of ~8.6 mg of salt/day.

The instrument vaporizer was cleaned at least every 200mg worth of salt injected.

505
- @ 35PSU & 2.2µl injections, this is 2597 salty injections, or 371 samples @ 7 injections each. (~ every 23 analytical days)

Finally, analytical data quality control was conducted in the following way

- The first injection of each sample was discarded, to minimize instrument memory issues
- If the standard deviation of the remaining 6 injections was >0.04‰, up to one outlier could be removed. Any
510 samples where the standard deviation of measured values was still >0.04‰ were rerun the following day from the same vial, using the same septa.
- If a rerun would not be possible the following day, the vial septa was replaced with a new one.
- Data from each hydrocast were inspected as a group. Any samples that appeared inconsistent with the rest of the hydrocast (e.g. with regards to salinity, or neighboring $\delta^{18}O$ values) were rerun. If the rerun occurred within 1 week
515 of the initial run, the same vial was used. Otherwise, a fresh aliquot of sample was drawn from the resealed serum vial.

Data availability

All data used in this study can be accessed at: https://doi.org/10.25740/zf704jg7109

Author contributions:

520 Conceptualization: RBD

Methodology: RBD, ANH, DAM

Investigation: ANH, DAM, RBD

Visualization: ANH

Funding acquisition: RBD

525 Project administration: RBD

Supervision: RBD

Writing – original draft: ANH

Writing – review & editing: ANH, SSJ, RBD, DAM, RAM

Contribution of data: ANH, DAM, RBD, SSJ, RAM

530

Competing interests

The authors declare that they have no conflict of interest.

Acknowledgments

References

Adusumilli, S., Fricker, H. A., Medley, B., Padman, L., and Siegfried, M. R.: Interannual variations in meltwater input to the
545   Southern Ocean from Antarctic ice shelves, Nat. Geosci., 13, 616–620, https://doi.org/10.1038/s41561-020-0616-z, 2020.

Assmann, K. M., Hellmer, H. H., and Jacobs, S. S.: Amundsen Sea ice production and transport, J. Geophys. Res. Oceans,
110, https://doi.org/10.1029/2004JC002797, 2005.

Belton, D. J., Deschaume, O., and Perry, C. C.: An overview of the fundamentals of the chemistry of silica with relevance to
biosilicification and technological advances, Febs J., 279, 1710–1720, https://doi.org/10.1111/j.1742-4658.2012.08531.x,
550   2012.

Benetti, M., Sveinbjörnsdóttir, A. E., Ólafsdóttir, R., Leng, M. J., Arrowsmith, C., Debondt, K., Fripiat, F., and Aloisi, G.:
Inter-comparison of salt effect correction for δ18O and δ2H measurements in seawater by CRDS and IRMS using the gas-
H2O equilibration method, Mar. Chem., 194, 114–123, https://doi.org/10.1016/j.marchem.2017.05.010, 2017.

Biddle, L. C., Heywood, K. J., Kaiser, J., and Jenkins, A.: Glacial Meltwater Identification in the Amundsen Sea, J. Phys.
555   Oceanogr., 47, 933–954, https://doi.org/10.1175/JPO-D-16-0221.1, 2017.

Biddle, L. C., Loose, B., and Heywood, K. J.: Upper Ocean Distribution of Glacial Meltwater in the Amundsen Sea,
Antarctica, J. Geophys. Res. Oceans, 124, https://doi.org/10.1029/2019JC015133, 2019.

Blunier, T. and Brook, E. J.: Timing of Millennial-Scale Climate Change in Antarctica and Greenland During the Last
Glacial Period, Science, 291, 109–112, https://doi.org/10.1126/science.291.5501.109, 2001.

560   Christie, F. D. W., Steig, E. J., Gourmelen, N., Tett, S. F. B., and Bingham, R. G.: Inter-decadal climate variability induces differential ice response along Pacific-facing West Antarctica, Nat. Commun., 14, 93, https://doi.org/10.1038/s41467-022-35471-3, 2023.

Coplen, T. B.: Reporting of stable hydrogen, carbon, and oxygen isotopic abundances (Technical Report), Pure Appl. Chem., 66, 273–276, https://doi.org/10.1351/pac199466020273, 1994.

565   Dierssen, H. M., Smith, R. C., and Vernet, M.: Glacial meltwater dynamics in coastal waters west of the Antarctic peninsula, Proc. Natl. Acad. Sci., 99, 1790–1795, https://doi.org/10.1073/pnas.032206999, 2002.

Donat-Magnin, M., Jourdain, N. C., Kittel, C., Agosta, C., Amory, C., Gallée, H., Krinner, G., and Chekki, M.: Future ice-sheet surface mass balance and melting in the Amundsen region, West Antarctica, The Cryosphere, https://doi.org/10.5194/tc-2020-113, 2020.

570   Donat-Magnin, M., Jourdain, N. C., Kittel, C., Agosta, C., Amory, C., Gallée, H., Krinner, G., and Chekki, M.: Future surface mass balance and surface melt in the Amundsen sector of the West Antarctic Ice Sheet, The Cryosphere, 15, 571–593, https://doi.org/10.5194/tc-15-571-2021, 2021.

Dotto, T. S., Naveira Garabato, A. C., Bacon, S., Holland, P. R., Kimura, S., Firing, Y. L., Tsamados, M., Wåhlin, A. K., and Jenkins, A.: Wind-Driven Processes Controlling Oceanic Heat Delivery to the Amundsen Sea, Antarctica, J. Phys.
575   Oceanogr., 49, 2829–2849, https://doi.org/10.1175/JPO-D-19-0064.1, 2019.

Dotto, T. S., Naveira Garabato, A. C. N., Wåhlin, A. K., Bacon, S., Holland, P. R., Kimura, S., Tsamados, M., Herraiz-Borreguero, L., Kalén, O., and Jenkins, A.: Control of the Oceanic Heat Content of the Getz-Dotson Trough, Antarctica, by the Amundsen Sea Low, J. Geophys. Res. Oceans, 125, e2020JC016113, https://doi.org/10.1029/2020JC016113, 2020.

Dutrieux, P., De Rydt, J., Jenkins, A., Holland, P. R., Ha, H. K., Lee, S. H., Steig, E. J., Ding, Q., Abrahamsen, E. P., and
580   Schroder, M.: Strong Sensitivity of Pine Island Ice-Shelf Melting to Climatic Variability, Science, 343, 174–178, https://doi.org/10.1126/science.1244341, 2014.

Epstein, S. and Mayeda, T.: Variation of 18O content of waters from natural sources, Geochem. Cosmochem. Acta, 4, 213–224, 1953.

Flexas, M. M., Thompson, A., Schodlok, M., Zhang, H., and Speer, K.: Antarctic Peninsula warming triggers enhanced basal
585   melt rates throughout West Antarctica, Sci. Adv., 12, 2022.

Fogwill, C. J., Phipps, S. J., Turney, C. S. M., and Golledge, N. R.: Sensitivity of the Southern Ocean to enhanced regional Antarctic ice sheet meltwater input, Earths Future, 3, 317–329, https://doi.org/10.1002/2015EF000306, 2015.

Fretwell, P., Pritchard, H. D., Vaughan, D. G., Bamber, J. L., Barrand, N. E., Bell, R., Bianchi, C., Bingham, R. G., Blankenship, D. D., Casassa, G., Catania, G., Callens, D., Conway, H., Cook, A. J., Corr, H. F. J., Damaske, D., Damm, V.,
590   Ferraccioli, F., Forsberg, R., Fujita, S., Gim, Y., Gogineni, P., Griggs, J. A., Hindmarsh, R. C. A., Holmlund, P., Holt, J. W., Jacobel, R. W., Jenkins, A., Jokat, W., Jordan, T., King, E. C., Kohler, J., Krabill, W., Riger-Kusk, M., Langley, K. A., Leitchenkov, G., Leuschen, C., Luyendyk, B. P., Matsuoka, K., Mouginot, J., Nitsche, F. O., Nogi, Y., Nost, O. A., Popov, S. V., Rignot, E., Rippin, D. M., Rivera, A., Roberts, J., Ross, N., Siegert, M. J., Smith, A. M., Steinhage, D., Studinger, M., Sun, B., Tinto, B. K., Welch, B. C., Wilson, D., Young, D. A., Xiangbin, C., and Zirizzotti, A.: Bedmap2: improved ice bed,
595   surface and thickness datasets for Antarctica, The Cryosphere, 7, 375–393, https://doi.org/10.5194/tc-7-375-2013, 2013.

Hellmer, H. H., Jacobs, S. S., and Jenkins, A.: Oceanic Erosion of a Floating Antarctic Glacier in the Amundsen Sea, in: Ocean, Ice, and Atmosphere: Interactions at the Antarctic Continental Margin, vol. 75, edited by: Jacobs, S. S. and Weiss, R. F., American Geophysical Union, Washington, D. C., 83–99, https://doi.org/10.1029/AR075p0083, 1998.

600 Heywood, K. J., Biddle, L., Boehme, L., Dutrieux, P., Fedak, M., Jenkins, A., Jones, R., Kaiser, J., Mallett, H., Naveira Garabato, A., Renfrew, I., Stevens, D., and Webber, B.: Between the Devil and the Deep Blue Sea: The Role of the Amundsen Sea Continental Shelf in Exchanges Between Ocean and Ice Shelves, Oceanography, 29, 118–129, https://doi.org/10.5670/oceanog.2016.104, 2016.

Holland, P. R., Bracegirdle, T. J., Dutrieux, P., Jenkins, A., and Steig, E. J.: West Antarctic ice loss influenced by internal climate variability and anthropogenic forcing, Nat. Geosci., 12, 718–724, https://doi.org/10.1038/s41561-019-0420-9, 2019.

605 IPCC: The Ocean and Cryosphere in a Changing Climate: Special Report of the Intergovernmental Panel on Climate Change, 1st ed., Cambridge University Press, https://doi.org/10.1017/9781009157964, 2022.

Jacobs, S. S., Fairbanks, R. G., and Horibe, Y.: Origin and evolution of water masses near the Antarctic continental margin: Evidence from H2 18O / H2 16O ratios in seawater, Oceanol. Antarct. Cont. Shelf, 43, 59–85, https://doi.org/10.1029/AR043, 1985.

610 Jacobs, S. S., Hellmer, H. H., and Jenkins, A.: Antarctic Ice Sheet melting in the southeast Pacific, Geophys. Res. Lett., 23, 957–960, https://doi.org/10.1029/96GL00723, 1996.

Jacobs, S. S., Giulivi, C. F., and Mele, P. A.: Freshening of the Ross Sea during the late 20th century., Science, 297, 386–389, https://doi.org/10.1126/science.1069574, 2002.

Jacobs, S. S., Giulivi, C. F., and Dutrieux, P.: Persistent Ross Sea Freshening from Imbalance West Antarctic Ice Shelf
615 Melting, J. Geophys. Res. Oceans, n/a, e2021JC017808, https://doi.org/10.1029/2021JC017808, 2022.

Jenkins, A., Dutrieux, P., Jacobs, S. S., McPhail, S. D., Perrett, J. R., Webb, A. T., and White, D.: Observations beneath Pine Island Glacier in West Antarctica and implications for its retreat, Nat. Geosci., 3, 468–472, https://doi.org/10.1038/ngeo890, 2010.

Jenkins, A., Shoosmith, D., Dutrieux, P., Jacobs, S. S., Kim, T. W., Lee, S. H., Ha, H. K., and Stammerjohn, S.: West
620 Antarctic Ice Sheet retreat in the Amundsen Sea driven by decadal oceanic variability, Nat. Geosci., 11, 733–738, https://doi.org/10.1038/s41561-018-0207-4, 2018.

Jeon, M. H., Jung, J., Park, M. O., Aoki, S., Kim, T.-W., and Kim, S.-K.: Tracing Circumpolar Deep Water and glacial meltwater using humic-like fluorescent dissolved organic matter in the Amundsen Sea, Antarctica, Mar. Chem., 235, 104008, https://doi.org/10.1016/j.marchem.2021.104008, 2021.

625 Joughin, I., Shapero, D., Smith, B., Dutrieux, P., and Barham, M.: Ice-shelf retreat drives recent Pine Island Glacier speedup, Sci. Adv., 7, eabg3080, https://doi.org/10.1126/sciadv.abg3080, 2021a.

Joughin, I., Shapero, D., Dutrieux, P., and Smith, B.: Ocean-induced melt volume directly paces ice loss from Pine Island Glacier, Sci. Adv., 7, eabi5738, https://doi.org/10.1126/sciadv.abi5738, 2021b.

Kim, T.-W., Yang, H. W., Dutrieux, P., Wåhlin, A. K., Jenkins, A., Kim, Y. G., Ha, H. K., Kim, C.-S., Cho, K.-H., Park, T.,
630 Park, J., Lee, S., and Cho, Y. K.: Interannual Variation of Modified Circumpolar Deep Water in the Dotson-Getz Trough, West Antarctica, J. Geophys. Res. Oceans, n/a, e2021JC017491, https://doi.org/10.1029/2021JC017491, 2021.

Kimura, S., Jenkins, A., Regan, H., Holland, P. R., Assmann, K. M., Whitt, D. B., Van Wessem, M., van de Berg, W. J., Reijmer, C. H., and Dutrieux, P.: Oceanographic Controls on the Variability of Ice-Shelf Basal Melting and Circulation of Glacial Meltwater in the Amundsen Sea Embayment, Antarctica, J. Geophys. Res. Oceans, 122, 10131–10155, 635 https://doi.org/10.1002/2017JC012926, 2017.

Leclerc, A. J. and Labeyrie, L.: Temperature dependence of the oxygen isotopic fractionation between diatom silica and water, Earth Planet. Sci. Lett., 84, 69–74, https://doi.org/10.1016/0012-821X(87)90177-4, 1987.

Lécuyer, C., Gardien, V., Rigaudier, T., Fourel, F., Martineau, F., and Cros, A.: Oxygen isotope fractionation and equilibration kinetics between CO_2 and H_2O as a function of salinity of aqueous solutions, Chem. Geol., 264, 122–126, 640 https://doi.org/10.1016/j.chemgeo.2009.02.017, 2009.

van der Linden, E. C., Le Bars, D., Lambert, E., and Drijfhout, S.: Calibration of basal melt on past ice discharge lowers projections of Antarctica's sea level contribution, Ice sheets/Antarctic, https://doi.org/10.5194/tc-2021-348, 2021.

van der Linden, E. C., Le Bars, D., Lambert, E., and Drijfhout, S.: Antarctic contribution to future sea level from ice shelf basal melt as constrained by ice discharge observations, The Cryosphere, 17, 79–103, https://doi.org/10.5194/tc-17-79-2023, 645 2023.

Mallett, H. K. W., Boehme, L., Fedak, M., Heywood, K. J., Stevens, D. P., and Roquet, F.: Variation in the Distribution and Properties of Circumpolar Deep Water in the Eastern Amundsen Sea, on Seasonal Timescales, Using Seal-Borne Tags, Geophys. Res. Lett., 45, 4982–4990, https://doi.org/10.1029/2018GL077430, 2018.

Mankoff, K. D., Jacobs, S. S., Tulaczyk, S. M., and Stammerjohn, S. E.: The role of Pine Island Glacier ice shelf basal 650 channels in deep-water upwelling, polynyas and ocean circulation in Pine Island Bay, Antarctica, Ann. Glaciol., 53, 123–128, https://doi.org/10.3189/2012AoG60A062, 2012.

Masson-Delmotte, V., Hou, S., Ekaykin, A., Jouzel, J., Aristarain, A., Bernardo, R. T., Bromwich, D., Cattani, O., Delmotte, M., Falourd, S., Frezzotti, M., Gallée, H., Genoni, L., Isaksson, E., Landais, A., Helsen, M. M., Hoffmann, G., Lopez, J., Morgan, V., Motoyama, H., Noone, D., Oerter, H., Petit, J. R., Royer, A., Uemura, R., Schmidt, G. A., Schlosser, E., 655 Simões, J. C., Steig, E. J., Stenni, B., Stievenard, M., van den Broeke, M. R., van de Wal, R. S. W., van de Berg, W. J., Vimeux, F., and White, J. W. C.: A Review of Antarctic Surface Snow Isotopic Composition: Observations, Atmospheric Circulation, and Isotopic Modeling*, J. Clim., 21, 3359–3387, https://doi.org/10.1175/2007JCLI2139.1, 2008.

Meredith, M. P., Brandon, M. A., Wallace, M. I., Clarke, A., Leng, M. J., Renfrew, I. A., van Lipzig, N. P. M., and King, J. C.: Variability in the freshwater balance of northern Marguerite Bay, Antarctic Peninsula: Results from δ18O, Deep-Sea 660 Res. II, 55, 309–322, https://doi.org/10.1016/j.dsr2.2007.11.005, 2008.

Meredith, M. P., Wallace, M. I., Stammerjohn, S. E., Renfrew, I. A., Clarke, A., Venables, H. J., Shoosmith, D. R., Souster, T., and Leng, M. J.: Changes in the freshwater composition of the upper ocean west of the Antarctic Peninsula during the first decade of the 21st century, Prog. Oceanogr., 87, 127–143, https://doi.org/10.1016/j.pocean.2010.09.019, 2010.

Meredith, M. P., Falk, U., Bers, A. V., Mackensen, A., Schloss, I. R., Ruiz Barlett, E., Jerosch, K., Silva Busso, A., and 665 Abele, D.: Anatomy of a glacial meltwater discharge event in an Antarctic cove, Philos. Trans. R. Soc. Math. Phys. Eng. Sci., 376, 20170163, https://doi.org/10.1098/rsta.2017.0163, 2018.

Naveira Garabato, A. C. N., Forryan, A., Dutrieux, P., Brannigan, L., Biddle, L. C., Heywood, K. J., Jenkins, A., Firing, Y. L., and Kimura, S.: Vigorous lateral export of the meltwater outflow from beneath an Antarctic ice shelf, Nature, 542, 219–222, https://doi.org/10.1038/nature20825, 2017.

670   Östlund, H. G. and Hut, G.: Arctic Ocean water mass balance from isotope data, J. Geophys. Res. Oceans, 89, 6373–6381, https://doi.org/10.1029/JC089iC04p06373, 1984.

Paolo, F. S., Fricker, H. A., and Padman, L.: Volume loss from Antarctic ice shelves is accelerating, Science, 348, 327–331, https://doi.org/10.1126/science.aaa0940, 2015.

Paolo, F. S., Padman, L., Fricker, H. A., Adusumilli, S., Howard, S., and Siegfried, M. R.: Response of Pacific-sector
675   Antarctic ice shelves to the El Niño/Southern Oscillation, Nat. Geosci., 11, 121–126, https://doi.org/10.1038/s41561-017-0033-0, 2018.

Paolo, F. S., Gardner, A., Greene, C., Nilsson, J., Schodlok, M., Schlegel, N., and Fricker, H.: Widespread slowdown in thinning rates of West Antarctic Ice Shelves, Ice sheets/Antarctic, https://doi.org/10.5194/egusphere-2022-1128, 2022.

Pritchard, H. D., Ligtenberg, S. R. M., Fricker, H. A., Vaughan, D. G., van den Broeke, M. R., and Padman, L.: Antarctic
680   ice-sheet loss driven by basal melting of ice shelves, Nature, 484, 502–505, https://doi.org/10.1038/nature10968, 2012.

Randall-Goodwin, E., Meredith, M. P., Jenkins, A., Yager, P. L., Sherrell, R. M., Abrahamsen, E. P., Guerrero, R., Yuan, X., Mortlock, R. A., Gavahan, K., Alderkamp, A.-C., Ducklow, H., Robertson, R., and Stammerjohn, S. E.: Freshwater distributions and water mass structure in the Amundsen Sea Polynya region, Antarctica, Elem. Sci. Anthr., 3, 000065, https://doi.org/10.12952/journal.elementa.000065, 2015.

685   Rignot, E. and Jacobs, S. S.: Rapid Bottom Melting Widespread near Antarctic Ice Sheet Grounding Lines, Science, 296, 2020–2023, https://doi.org/10.1126/science.1070942, 2002.

Rignot, E., Velicogna, I., Van Den Broeke, M. R., Monaghan, A., and Lenaerts, J.: Acceleration of the contribution of the Greenland and Antarctic ice sheets to sea level rise, Geophys. Res. Lett., 38, 1–5, https://doi.org/10.1029/2011GL046583, 2011.

690   Rignot, E., Mouginot, J., Scheuchl, B., van den Broeke, M., van Wessem, M. J., and Morlighem, M.: Four decades of Antarctic Ice Sheet mass balance from 1979–2017, Proc. Natl. Acad. Sci., 116, 1095–1103, https://doi.org/10.1073/pnas.1812883116, 2019.

Rohling, E. J.: PALEOCEANOGRAPHY, PHYSICAL AND CHEMICAL PROXIES | Oxygen Isotope Composition of Seawater, in: Encyclopedia of Quaternary Science, Elsevier, 915–922, https://doi.org/10.1016/B978-0-444-53643-3.00293-4,
695   2013.

Rubin, S. I., Takahashi, T., Chipman, D. W., and Goddard, J. G.: Primary productivity and nutrient utilization ratios in the Pacific sector of the Southern Ocean based on seasonal changes in seawater chemistry, Deep Sea Res. Part Oceanogr. Res. Pap., 45, 1211–1234, https://doi.org/10.1016/S0967-0637(98)00021-1, 1998.

Schaffer, J., Timmermann, R., Arndt, J. E., Steinhage, D., and Kanzow, T.: RTopo-2: A global dataset of ice sheet
700   topography, cavity geometry and ocean bathymetry to study ice-ocean interaction in Northeast Greenland, in: EPIC3REKLIM conference "Our Climate - Our Future", Berlin, Germany, 2014-10-06-2014-10-09, REKLIM conference "Our Climate - Our Future," Berlin, Germany, 2014.

Schneider, D. P., Steig, E. J., van Ommen, T. D., Dixon, D. A., Mayewski, P. A., Jones, J. M., and Bitz, C. M.: Antarctic temperatures over the past two centuries from ice cores, Geophys. Res. Lett., 33, https://doi.org/10.1029/2006GL027057,
705   2006.

Shepherd, A., Gilbert, L., Muir, A. S., Konrad, H., McMillan, M., Slater, T., Briggs, K. H., Sundal, A. V., Hogg, A. E., and Engdahl, M. E.: Trends in Antarctic Ice Sheet Elevation and Mass, Geophys. Res. Lett., 46, 8174–8183, https://doi.org/10.1029/2019GL082182, 2019.

710 Silvano, A., Rintoul, S. R., Peña-Molino, B., Hobbs, W. R., Wijk, E. van, Aoki, S., Tamura, T., and Williams, G. D.: Freshening by glacial meltwater enhances melting of ice shelves and reduces formation of Antarctic Bottom Water, Sci. Adv., 4, eaap9467, https://doi.org/10.1126/sciadv.aap9467, 2018.

Skrzypek, G. and Ford, D.: Stable Isotope Analysis of Saline Water Samples on a Cavity Ring-down Spectroscopy Instrument, Environ. Sci. Technol., 48, 2827–2834, https://doi.org/10.1021/es4049412, 2014.

Steig, E. J., Mayewski, P. A., Dixon, D. A., Kaspari, S. D., Frey, M. M., Schneider, D. P., Arcone, S. A., Hamilton, G. S.,
715 Blue Spikes, V., Mary Albert, Meese, D., Gow, A. J., Shuman, C. A., White, J. W. C., Sneed, S., Flaherty, J., and Wumkes, M.: High-resolution ice cores from US ITASE (West Antarctica): development and validation of chronologies and determination of precision and accuracy, Ann. Glaciol., 41, 77–84, https://doi.org/10.3189/172756405781813311, 2005.

Tamsitt, V., England, M. H., Rintoul, S. R., and Morrison, A. K.: Residence time and transformation of warm Circumpolar Deep Water on the Antarctic continental shelf, Geophys. Res. Lett., e2021GL096092,
720 https://doi.org/10.1029/2021GL096092, 2021.

Thomas, E. R., Dennis, P. F., Bracegirdle, T. J., and Franzke, C.: Ice core evidence for significant 100-year regional warming on the Antarctic Peninsula, Geophys. Res. Lett., 36, https://doi.org/10.1029/2009GL040104, 2009.

Thurnherr, A. M., Jacobs, S. S., Dutrieux, P., and Giulivi, C. F.: Export and circulation of ice cavity water in Pine Island Bay, West Antarctica, J. Geophys. Res. Oceans, 119, 1754–1764, https://doi.org/10.1002/2013JC009307, 2014.

725 Velicogna, I., Sutterley, T. C., and Broeke, M. R. van den: Regional acceleration in ice mass loss from Greenland and Antarctica using GRACE time-variable gravity data, Geophys. Res. Lett., 41, 8130–8137, https://doi.org/10.1002/2014GL061052, 2014.

Wåhlin, A. K., Graham, A. G. C., Hogan, K. A., Queste, B. Y., Boehme, L., Larter, R. D., Pettit, E. C., Wellner, J., and Heywood, K. J.: Pathways and modification of warm water flowing beneath Thwaites Ice Shelf, West Antarctica, Sci. Adv.,
730 7, eabd7254, https://doi.org/10.1126/sciadv.abd7254, 2021.

Walker, S. A., Azetsu-Scott, K., Normandeau, C., Kelley, D. E., Friedrich, R., Newton, R., Schlosser, P., McKay, J. L., Abdi, W., Kerrigan, E., Craig, S. E., and Wallace, D. W. R.: Oxygen isotope measurements of seawater (H2 18O/H2 16O): A comparison of cavity ring-down spectroscopy (CRDS) and isotope ratio mass spectrometry (IRMS), Limnol. Oceanogr. Methods, 14, 31–38, https://doi.org/10.1002/lom3.10067, 2016.

735 WCRP Global Sea Level Budget Group: Global sea-level budget 1993–present, Earth Syst. Sci. Data, 10, 1551–1590, https://doi.org/10.5194/essd-10-1551-2018, 2018.

Webber, B. G. M., Heywood, K. J., Stevens, D. P., Dutrieux, P., Abrahamsen, E. P., Jenkins, A., Jacobs, S. S., Ha, H. K., Lee, S. H., and Kim, T. W.: Mechanisms driving variability in the ocean forcing of Pine Island Glacier, Nat. Commun., 8, 14507, https://doi.org/10.1038/ncomms14507, 2017.

740